Universität Bonn

Physikalisches Institut

Search for Charged-Lepton Flavour Violation in Top-Quark Decays in the $\mu\ \tau$ Channel using the ATLAS Detector at the LHC

Arshia Ruina

This analysis presents a first direct search for charged-lepton flavour violation in top-quark decays to the $\mu\tau$ final state using data collected from proton-proton collisions at the LHC, during the years 2015 and 2016, at a centre-of-mass energy of $\sqrt{s} = 13$ TeV, corresponding to an integrated luminosity of 36.1 fb^{-1}, as detected by the ATLAS experiment. The search is performed by studying top-quark pair events where one quark undergoes a flavour-violating decay $t(\bar{t}) \to \ell^{\pm}\ell'^{\mp}q(\overline{q})$, where $q \in \{u, c\}$ and $\ell \in \{\mu, \tau\}$ while the other top decays according to the SM into a b-quark and a leptonically-decaying W-boson. Data is found to be compatible with the absence of a signal and a fit to the background is performed using the profile likelihood technique. The observed (expected) upper limit on the branching ratio of $t_{\mathrm{LFV}} \to \mu\tau q$ is set to $0.96(1.00) \times 10^{-4}$ at the 95% confidence level using the modified frequentist approach.

CERN-THESIS-2018-315
08/10/2018

Physikalisches Institut der
Universität Bonn
Nussallee 12
D-53115 Bonn

BONN-IB-2019-001
October 2018

Universität Bonn

Physikalisches Institut

Search for Charged-Lepton Flavour Violation in Top-Quark Decays in the $\mu\ \tau$ Channel using the ATLAS Detector at the LHC

Arshia Ruina

Dieser Forschungsbericht wurde als Masterarbeit von der Mathematisch-Naturwissenschaftlichen Fakultät der Universität Bonn angenommen.

Angenommen am:	12.10.2018
1. Gutachter:	Priv. Doz. Dr. Markus Cristinziani
2. Gutachter:	Prof. Dr. Norbert Wermes

Acknowledgements

I would like to thank my thesis supervisor, Priv. Doz. Dr. Markus Cristinziani, for giving me the opportunity to work in the ERC Top Couplings Group at the Physikalisches Institut (PI) of Uni Bonn, thereby introducing me to the exciting field of top quark physics. His encouragement and guidance throughout my thesis helped me strengthen my weak areas and propelled me to work harder. His foresight was pivotal in planning out the work of my thesis. I would also like to thank Prof. Dr. Norbert Wermes for hosting our group in PI Uni Bonn and for agreeing to be my second supervisor. He has been a mentor and an immense source of motivation throughout my graduate studies.

I'd like to thank all the group members for welcoming me to a friendly and international atmosphere. All the helpful discussions and constructive criticism, not only during weekly meetings but also whenever I needed them, helped me immensely in my work. Special thanks to Carlo A. Gottardo for his expert guidance and patience throughout my thesis. I am grateful to him for helping me with understanding the experimental and theoretical aspects of my analysis, assisting me through programming and computing difficulties, guiding me with data analysis tools, taking the time out to review my thesis and being patient with my questions. I have constantly been able to draw inspiration from his hard work, efficiency and dedication. I'd like to thank Dr. Julien Caudron (currently employed at Energy Systems Catapult, Birmingham) and Sebastian Heer for always having the patience to answer questions, no matter how trivial they were. I also owe my gratitude to Dr. Vadim Kostyukhin and Andrea Sciandra for their invaluable help and suggestions at various stages of my work and Dr. David Hohn for assisting me in understanding parts of the ttH analysis that were relevant to my work. A big thank you to my colleague Ö. Oğul Öncel who often helped me with debugging, discussing physics concepts and having conversations that were beyond the scope of high-energy particle physics. Also, thanks to Sebastian, Oğul and especially Carlo for their comments and suggestions that helped me prepare for my colloquium.

The successful completion of this thesis is also attributed to the Bonn-Cologne Graduate School of Physics and Astronomy's Honors programme, PI's IT-support team and to the ATLAS Secretariat at CERN, for providing prompt help whenever it was needed. Many thanks to Prof. Dr. Ian Brock and his group for maintaining and sharing the templates and instructions for preparing theses in LaTeX [1]. I'd also like to thank B. S. Vasanth for offering his help in proof-reading the thesis.

I made some really wonderful friends during my stay in Bonn who became my family away from home. I thank them all for having played a huge part in making my life stress-free and fun-filled throughout this period. My heartfelt gratitude goes out to Arka Mallick who helped me cope with challenging times by bringing in lots of love and laughter.

I am eternally grateful to my parents who have been my rock-solid pillars of support despite being hundreds of miles away. Their love for and faith in me have given me the strength to overcome obstacles and to keep moving forward. Mere words cannot do justice to acknowledging all that they have done for me.

Contents

CHAPTER 1

Introduction

"We are at the very beginning of time for the human race. It is not unreasonable that we grapple with problems. But there are tens of thousands of years in the future. Our responsibility is to do what we can, learn what we can, improve the solutions, and pass them on."

-Richard P. Feynman

For more than two thousand years, people have wondered about the world around them and have been fascinated by the behaviour of Nature and its numerous components. Such a curiosity has constantly kept the pot boiling about the fundamental building blocks of matter and their interactions. The foundation of the fundamental principles of physics such as the atomic theory was laid by the ancient Greeks and ever since, the field has been developing in varied paces over the centuries. A scientific and philosophical upheaval was caused by Copernicus' proposed heliocentric model following which Galileo Galilei brought forth the concept of scientific method that involved rigorous testing of scientific theories prior to their acceptance. Classical mechanics became a tried-and-tested discipline that revolutionised science and its technological applications. The atom was found to be no longer the indivisible building block of matter but made out of certain positive and negative components.

However, despite what most scientists believed to be the absolute explanation for everything, classical theory was incapable of explaining certain observations, thereby paving the way for the ground-breaking concepts of the quantum nature of radiation, thanks to Max Planck, and Einstein's theory of relativity. Within the first-half of the twentieth century, the atomic substructure became well-established and advances in technology led to the discoveries of a plethora of new particles in the second-half. Three families of quarks and leptons were discovered and their interactions were studied in great detail, all of which ultimately led to the Standard Model (SM) of particle physics, as we know it today.

Modern particle physics deals with a property of particles called "flavour" which identifies its species. Quarks and leptons each comprise six flavours and a "symmetry" of this property exists when particles of different flavours can be interchanged in certain interactions without affecting the physics. The flavour of both, charged and neutral leptons, is conserved according to the SM. Nonetheless, observations have been made where transformations between neutrino flavour states occurred which indicates the existence of some New Physics. While the SM has been extremely successful in making numerous predictions over the years, e.g. the existence of the top quark, the tau-lepton, the Higgs boson and many others, it does not tell us the entire story. In fact, the SM does not explain observed phenomena like the neutrino masses or oscillations, dark matter, dark energy or the force of gravitation. Beyond-the-SM physics are being looked out for and theories are being proposed in order to explain such experimental observations. A minimal extension of the SM which allows neutrino oscillations to occur also permits a non-conservation of flavour for charged leptons. However, the rates of charged-lepton flavour-violating processes that arise from such extensions of the SM are currently beyond experimental sensitivity.

In this thesis, a model-independent approach using an effective field theory (EFT) is considered where two-lepton, two-quark interactions undergoing charged-lepton flavour violation (cLFV) are studied. A search for cLFV in the decays of a top-quark into an electron, a muon and a light quark (u or c) has been extensively covered in Reference [2]. For the work of this thesis, the search is focussed on top-quark decays into a muon, a τ-lepton and a light quark. Figure 1.1 shows an example of such a decay where a pair of top-quarks are present such that one decays according to the SM (denoted as t_{SM}) into a b-quark and a W-boson (which further decays into two leptons) while the other (denoted as t_{LFV}) decays in the lepton-flavour violating mode. The top quark, being the heaviest of quarks and having a very short lifetime, has unique properties that makes it interesting for various physics studies. The decay channel with a τ-lepton and a muon are particularly interesting as the EFT coupling strengths involving a τ-lepton are weakly constrained while the muon offers greater sensitivity to cLFV searches. This study is performed using proton-proton collision data collected by the ATLAS detector at the LHC at CERN, Geneva during the years 2015 and 2016.

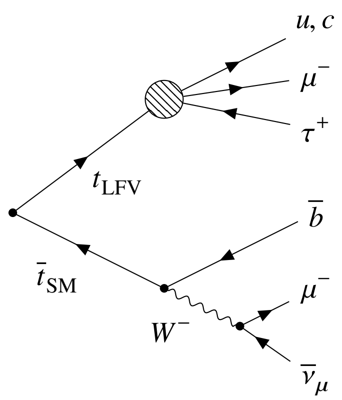

Figure 1.1: Example Feynman diagram for the process under study. [3]

The chapters of the thesis are organized as follows: the theoretical framework that supports this analysis is presented in Chapter 2. The data was provided by the ATLAS detector whose layout is described in Chapter 3. The analysis setup is outlined in Chapter 4 which is followed by a detailed account of the analysis strategy in Chapter 5. The results of the search are reported in Chapter 6 while Chapter 7 concludes the thesis.

CHAPTER 2

Theory

Particle physics deals with the fundamental constituents of the Universe and the interactions between them. These elementary particles and the force mediators between them are contained in what we call the Standard Model (SM) of particle physics. An overview of the SM and its constituents commences this chapter and is followed by a description of the idea of flavour in particle physics, the phenomenon of flavour mixing in the quark sector and flavour oscillations in neutrinos. The focus of this thesis is on charged-lepton flavour violation (cLFV) which has been approached using an effective field theory (EFT). In particular, cLFV is searched for in top-quark decays, taking advantage of their abundant production at the LHC, using data from the ATLAS detector. cLFV and its search using an EFT are described in Sections 2.5 and 2.6, followed by a section dedicated to the top quark. A brief account of the statistical analysis performed in order to test the presence of a signal (including the profile likelihood fit method) and handle the uncertainties is presented at the end of this chapter in Section 2.8. Theoretical concepts in this section closely follow from references [4] and [5].

2.1 The Standard Model

The SM arose in the 1960s from the contributions of Glashow, Weinberg and Salam [6–8] to the unification of the electromagnetic and weak interactions into the so-called electroweak theory and later additions of the strong interactions and the Higgs mechanism. The four fundamental forces of nature are the electromagnetic force, the weak force, the strong force and gravity, of which the SM describes three; the quantum field theories of gravity break down near the Planck scale and therefore cannot explain the very early Universe. The contents of the SM are shown in Figure 2.1 and are described below.

Fermions Leptons and quarks are fermions with a fractional intrinsic spin of 1/2 and are collectively called the "matter particles" and they make up the building blocks of all matter. Fermions follow the Fermi-Dirac statistics. Also, each fermion has its own antiparticle. There are twelve of them in the SM classified as quarks and leptons. They are also grouped in three generations where each successive generation is heavier by mass. The first generation of charged fermions are the lightest and represent the basic building blocks of the low-energy Universe [9].

- Quarks are grouped into three generations of up- and down-type quarks. The up (u), charm (c) and top (t) are up-type quarks with an electrical charge of +2/3 that belong to the first, second and

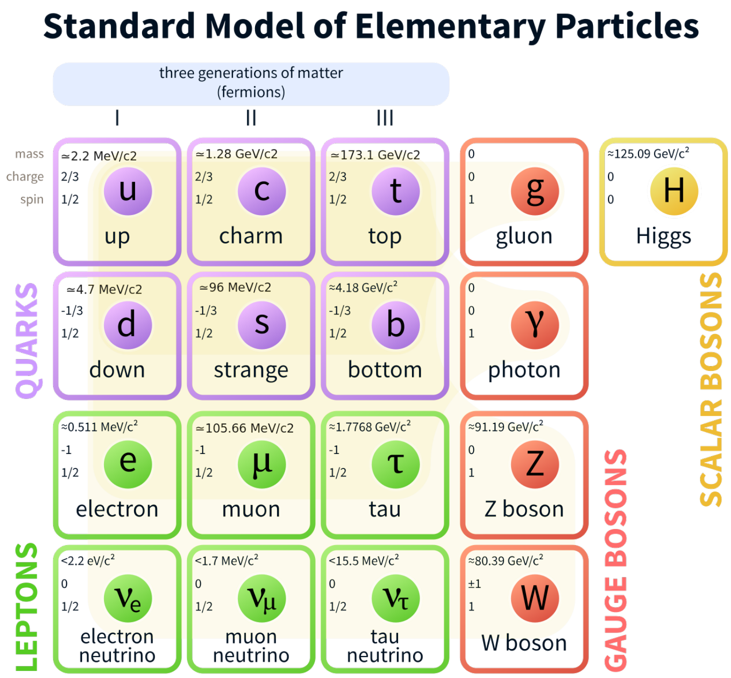

Figure 2.1: Particles of the Standard Model

third generations, respectively. The down (d), strange (s) and bottom (b) are down-type quarks with electrical charge of -1/3 and similarly grouped into the first, second and third respective generations. Besides, they possess weak isospin, which enables them to undergo electromagnetic and weak interactions. They also carry colour charge which allows them to interact via the strong force which is governed by Quantum Chromodynamics (QCD). Asymptotic freedom and colour confinement are two features of QCD – the former is a property of the theory that causes the coupling between particles to become weaker with an increase in energy while the latter implies that at low energies, quarks exist only in "colourless" bound states as hadrons[1] and not independently. The top quark is the heaviest of all which lends it some special properties and is discussed further in Section 2.7.

- Leptons are also grouped into three generations and two types – electrically charged and neutral. In the charged sector, exist the electron (e), muon (μ) and the tau-lepton (τ-lepton) belonging to the first, second and third generation, respectively, each carrying a charge of -1. They also have isospin and can interact via the weak force. The neutral sector consists of their corresponding neutrinos which are nearly massless and in the absence of electric charge on them, interact only via the weak force which makes them very difficult to detect. The leptons do not carry colour charge and are not affected by the strong force.

Gauge Bosons The gauge bosons are spin-1 particles which are referred to as the "force carriers" as

[1] Hadrons can be of two types, namely a *meson* and a *baryon*. Mesons are a combination of a quark and an anti-quark which essentially carry opposite colour charges that cancel each other out and make the meson colour-neutral. Baryons are a combination of three quarks which have three different colours and are thereby rendered colourless.

are they are the mediators of the three forces relevant to particle physics, namely the strong, weak and electromagnetic forces.

- The gluons (eight in total) are massless and are responsible for mediating the strong force among particles that carry the colour charge, namely quarks. The gluons themselves also carry the colour charge implying that they also undergo self-interaction.
- The photon is also massless and is the carrier of the electromagnetic force between electrically charged particles.
- The massive $W^{\pm}$ and Z^0 bosons are the weak force mediators and hence interact with all the quarks and leptons.

Higgs boson The Higgs boson is a scalar spin-0 particle, the only fundamental scalar discovered to date [9]. It was discovered most recently in 2012 by the ATLAS and CMS experiments at the LHC and has a mass of 125 GeV. It is responsible for the mechanism by which all other particles obtain mass. Quantum field theory describes particles as excitations in a field and fields that correspond to the fundamental fermions and bosons have zero vacuum expectation values. The Higgs field, on the contrary, has a non-zero vacuum expectation value which interacts with the other particles and gives them their masses.

According to the classical theory, elementary particles are treated as point particles. However, in quantum field theory, which is the basis of the SM, they are nothing but excitations in a quantum field and are governed by equations of motion given by the SM Lagrangian density $\mathcal{L}$.

2.2 Flavour

The concept of flavour lies in the very presence of three copies for each of the four types of fermions (up-type and down-type quarks, charge and neutral leptons) in the SM. In the initial years, the discovery of parity violation eventually led to the idea of a second neutrino (now referred to as the muon neutrino) which was later confirmed by the scattering of neutrinos coming from pion decays that produced only muons and no electrons ([10] and references therein). The decays of neutral kaons and the observation of CP-violation in them led to the speculation of a second and third generation of quarks, respectively, where the latter was supported by the discovery of the τ-lepton. In the years that followed, the discoveries of the b-quark, the t-quark and the ν_τ completed the flavour picture of elementary fermions.

2.3 Flavour Mixing in Quarks

The study of the nuclear β-decay led to the observation of differences in coupling strengths not only between quarks and leptons but also between the $u - d$ and $u - s$ weak interaction vertices. These observations were later accounted for by the Cabibbo hypothesis according to which the strengths of weak interactions for leptons did not vary from that of quarks but there existed a difference between the weak eigenstates (denoted as d' and s') and mass-eigenstates (denoted as d and s) of the quarks and are related to each other by a unitary matrix as shown in Equation 2.1 where θ_c is the Cabibbo angle.

$$\begin{pmatrix} d' \\ s' \end{pmatrix} = \begin{pmatrix} \cos\theta_c & \sin\theta_c \\ -\sin\theta_c & \cos\theta_c \end{pmatrix} \begin{pmatrix} d \\ s \end{pmatrix} \tag{2.1}$$

The Cabibbo mechanism is, naturally, extended to the third generation of quarks via the CKM matrix and is represented in Equation 2.2.

$$\begin{pmatrix} d' \\ s' \\ b' \end{pmatrix} = \begin{pmatrix} V_{ud} & V_{us} & V_{ub} \\ V_{cd} & V_{cs} & V_{cb} \\ V_{td} & V_{ts} & V_{tb} \end{pmatrix} \begin{pmatrix} d \\ s \\ b \end{pmatrix} \tag{2.2}$$

The elements of this matrix correspond to the relative strength of the interactions between the quarks. Due to the off-diagonal terms being relatively small, the matrix is nearly diagonal which implies that weak interactions of quarks from different generations is suppressed as compared to those of $u - d$, $c - s$ and $t - b$.

2.4 Neutral Lepton Flavour Violation

The flavour of a neutrino is determined by the lepton flavour produced in a charged-current (CC) weak interaction. This is also the principle that underlies neutrino detection. Initially, in the framework of the SM, it was assumed that neutrinos are massless particles and their flavours are invariant. However, this theory was incapable of explaining the solar neutrino problem observed since the mid-1960s. It was finally resolved on the basis of neutrino oscillations, which had been proposed by Bruno Pontecorvo in 1957. The following overview on neutrino oscillation is inspired from Reference [9].

Neutrino oscillations successfully explain the flavour transformations that were observed by the Sudbury National Observatory [11], the Super-Kamiokande experiment [12] and other experiments. The neutrino mass eigenstates (the fundamental particles) are labelled as ν_1, ν_2 and ν_3 which are different from their flavour eigenstates ν_e, ν_μ and ν_τ. They are related to each other by a unitary matrix U, also known as the Pontecorvo-Maki-Nakagawa-Sakata (PMNS) matrix for the mixing of neutrino states, as shown in Equation 2.3.

$$\begin{pmatrix} \nu_e \\ \nu_\mu \\ \nu_\tau \end{pmatrix} = \begin{pmatrix} U_{e1} & U_{e2} & U_{e3} \\ U_{\mu 1} & U_{\mu 2} & U_{\mu 3} \\ U_{\tau 1} & U_{\tau 2} & U_{\tau 3} \end{pmatrix} \begin{pmatrix} \nu_1 \\ \nu_2 \\ \nu_3 \end{pmatrix} \tag{2.3}$$

Hence, the three neutrino states that interact with the charged leptons via weak interactions are each a different superposition of the three neutrino states of definite mass. In other words, a neutrino propagates as a coherent linear superposition of the three mass eigenstates until it interacts and the wave function collapses into a weak flavour eigenstate, generating a charged lepton of the corresponding flavour. Neutrino oscillations occur when phase dissimilarities arise between the various components of the wave function due to differences in the masses of ν_1, ν_2 and ν_3. The probabilities of neutrino oscillations depend on the differences of the squared neutrino masses which have been determined by experiments but only upper limits have been put on the individual masses of the neutrinos.

2.5 Charged Lepton Flavour Violation

As was mentioned earlier, the SM was originally formulated with neutrinos assumed to be massless. In such a framework, charged-lepton flavour violation (cLFV) is strictly forbidden. However, evidence for neutrino oscillations showed that flavour transformations in neutrinos are possible, provided that they are not massless. A minimal extension of the SM, made by introducing right-handed Dirac neutrinos, that generates the required neutrino mass terms in the Lagrangian also allows cLFV. Nevertheless, with massive neutrinos (making no assumption on the mechanism of mass generation), cLFV processes are suppressed by the extremely tiny (differences of squared) masses of the neutrinos because of a GIM-like [13] suppression $\propto (\Delta m_{ij}/m_W)^4$. For example, the decay of a muon into an electron and a photon has a predicted branching ratio of $\mathcal{O}(10^{-55})$ [14] which is inaccessible to present and future experiments. This implies that observation of cLFV would be an unequivocal indication of New Physics (NP).

An underlying theoretical framework is of utmost importance in order to be able to interpret experimental data for cLFV searches. Neutrino mass can be generated in two ways: either by introducing right-handed neutrinos or by considering non-renormalisable operators [10]. For the first way, besides the problem of unreachable sensitivities mentioned above, the Yukawa couplings of the corresponding Dirac mass term is of $\mathcal{O}(10^{-12})$ [15]. The second way is the approach via an effective field, as described in the next section.

2.6 An Effective Approach

A model-independent approach by means of an effective field theory is considered where cLFV interactions are parameterised by higher-order non-renormalisable operators. The effective Lagrangian is then given by Equation 2.4 where it is expressed as a sum of the SM Lagrangian $\mathcal{L}^{\text{SM}}$ of dimension $d = 4$ and terms of higher orders.

$$\mathcal{L}^{\text{eff}} = \mathcal{L}^{\text{SM}} + \sum_{n\geq 1} C_{ij}^{4+n} \frac{1}{\Lambda^n} \mathcal{O}_{ij}^{4+n} \tag{2.4}$$

Here, Λ denotes the scale of NP and C and $\mathcal{O}$ are the effective couplings and operators. There exists only one possible $d = 5$ operator, called the Weinberg operator, after imposing the SM gauge symmetry constraints [16] which, however, violates lepton number. It is also a source of Majorana[2] neutrinos and leads to energy scales of $\Lambda > 10^{14}$ TeV in order to generate neutrino masses $M_\nu < 1$ eV. Alternatively, assuming that neutrino masses are generated by some other mechanism and placing the requirement of lepton number conservation on the effective operators, the term of $d = 6$ dimension turns out to be the first correction that parameterizes NP. The complete set of $d = 6$ operators is quite large but among them are present some four-fermion operators that can be responsible for cLFV processes.

Constraints on such two-lepton, two-quark interactions are listed in Reference [17]. Operators that involve top-quarks are weakly constrained which makes cLFV decays of the top-quark within the sensitivity of the LHC [18]. For the purpose of the search presented in this thesis, the decay channel involving a muon and a τ-lepton are chosen because of the high sensitivity of muons towards cLFV

[2] A Majorana fermion is one that is its own anti-particle.

searches and the relatively loose bounds on the operator coefficients that include the τ-lepton.

2.7 The Top Quark

The top quark was predicted by Makoto Kobayashi and Toshihide Maskawa in the early 1970s in order to solve the problem of CP-violation in kaon decays [19] and was discovered around twenty years later by the CDF and DØ experiments at Fermilab [20, 21]. The top quark belongs to the third generation of quarks and is the heaviest with a mass of (173.0 ± 0.4) GeV [22]. Its high mass leads to a Yukawa coupling with a value very close to one which makes the top quark an interesting probe into physics issues that cannot be explained by the SM [23]. It also has a very short lifetime $\approx 5.0 \times 10^{-25}$ s which is twenty times smaller than the timescale of strong interactions. This leads to a decay of the quark before it can undergo hadronisation which is the processes of quarks combining together to form hadrons. As a result, information about the top quark, unlike other quarks, can be extracted directly from its decay products.

The proton-proton collisions at the LHC result in a copious production of top quarks where they have become tools for searches of NP e.g. the search for exotic decays, for measurements of top-quark couplings to gauge bosons, or for the investigation of the proton structure [24]. They are produced dominantly as top-anti-top $t\bar{t}$ pairs either originating from quark-anti-quark ($q\bar{q}$) annihilation or gluon fusion as shown in Figure 2.2. The production mode of $q\bar{q}$ annihilation is caused by collisions of the valence quarks in the protons. However, at the LHC, which operates at a centre-of-mass energy of 13 TeV, gluon fusion is the dominant mode of production of $t\bar{t}$ pairs (80-90%).

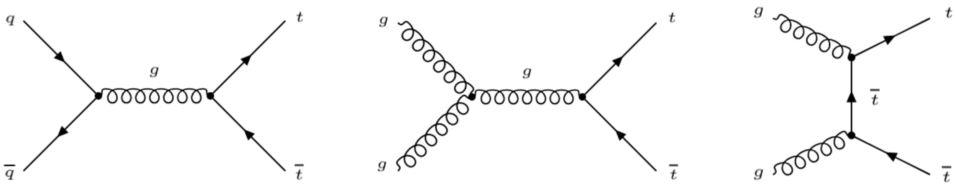

(a) $q\bar{q}$ annihilation (b) gluon fusion (s-channel) (c) gluon fusion (t-channel)

Figure 2.2: Production modes of a $t\bar{t}$ pair.

The top-quark decays predominantly into a W-boson and a b-quark with a measured branching ratio of about $(96 \pm 3)\%$ [22] where the W-boson can decay either leptonically ($W \to \ell\nu_\ell$ 33%) or hadronically (68%) while the b-quark hadronises in most cases. Final states of a $t\bar{t}$ decay can, therefore, be combinations of the decays of the two W-bosons present – fully hadronic, leptons+jets and dileptonic. Moreover, within these categories, further classification can be made depending on whether the τ-lepton decays leptonically ($\approx 35\%$) or hadronically ($\approx 65\%$).

2.8 Statistical Analysis

In an analysis, a fit is done to either compare distributions of variables with those expected from theory or to extract from them physical quantities of interest. In order to make a fit, the three important steps are (i) to define a hypothesis, which can be a function y depending on a variable or a set of variables x given a set of parameters θ, (ii) to define a test statistic, which is a variable depending on data such that if the hypothesis is correct, will have a known distribution function and (iii) to obtain estimates of the parameters and their uncertainties that give the best possible agreement between the data and theory. The actual value of the test statistic is then evaluated and if it lies in a region of high probability in the distribution function, it is concluded that the experiment corroborates the theory, whereas, if it lies in a region of low probability, it is concluded that the experiment refutes the theory or a parameter region that provides acceptable agreement has not been found.

The test statistics used here, commonly used by HEP experiments, is the profile likelihood ratio.

2.8.1 Profile Likelihood Ratio

Let us consider a binned analysis, where certain kinematic variables are measured for each selected event and are represented as histograms. If we construct such a histogram $\mathbf{n} = (n_1, \ldots, n_N)$ for a variable in the signal sample, the expectation value of n_i is given by

$$E[n_i] = \mu s_i + b_i \tag{2.5}$$

where s_i and b_i are the mean number of entries in the ith bin from signal and background respectively and the parameter μ represents the strength of the signal process, where a value of zero corresponds to a background-only hypothesis and a value of one corresponds to the nominal signal hypothesis.

Besides containing parameters of interest, e.g. the rate of the signal process (cross-section), the signal and background models will also contain certain *nuisance parameters*. These are parameters, denoted by θ, whose values affect the distribution of the observations but by themselves are not necessarily of interest. They are not known *a priori* but are fitted from data. Measurements can be made in control regions, that are composed of mostly background, in order to constrain the nuisance parameters by constructing a histogram $\mathbf{m} = (m_1, \ldots, m_M)$ of a certain variable where the expectation value of m_i is given by

$$E[m_i] = u_i(\theta) \tag{2.6}$$

where u_i are calculable quantities dependent on the nuisance parameters. The likelihood function (Equation 2.7) is then expressed as the product of Poissonian probabilities for all bins [4]

$$L(\mu, \theta) = \prod_{j=1}^{N} \frac{(\mu s_j + b_j)^{n_j}}{n_j!} \exp^{-(\mu s_j + b_j)} \prod_{k=1}^{M} \frac{u_k^{m_k}}{m_k!} \exp^{-u_k} \tag{2.7}$$

The profile likelihood ratio is then given by

$$\lambda(\mu) = \frac{L(\mu, \hat{\hat{\theta}})}{L(\hat{\mu}, \hat{\theta})} \tag{2.8}$$

to test a hypothesized value of μ, where in the numerator, $\hat{\hat{\theta}}$ is the value of θ that maximizes L for a fixed μ and in the denominator, $\hat{\mu}$ and $\hat{\theta}$ maximize L. Here, $0 \leq \lambda \leq 1$, with λ close to one implying good agreement between the data and the hypothesized value of μ and a convenient test statistic is defined as

$$t_\mu = -2 \ln \lambda(\mu) \tag{2.9}$$

CHAPTER 3

The LHC and the ATLAS Detector

This chapter gives a brief introduction to the physics of particle colliders in Section 3.1, the Large Hadron (LHC) at CERN in Section 3.2 and one of its four major experiments, A Toroidal LHC Apparatus (ATLAS) in Section 3.3. The ATLAS coordinate system and the major components of the detector, namely, the Inner Detector (ID), the calorimetry system, the muon spectrometer system and the magnet system are described in the last section, followed by a short note on the Trigger and Data Acquisition (TDAQ) system.

3.1 Physics of Particle Colliders

Particle accelerators can be of two types: (i) fixed-target experiments, where a beam of particles is made incident on a stationary target and (ii) collider experiments, where two accelerated beams of particles are made to collide [9]. Massive particles can only be produced when the energy in the centre-of-mass reference frame is larger than the mass of the particles. The centre-of-mass energy (E_{CM}) for a system of two colliding particles is given by:

$$E_{\mathrm{CM}} = \sqrt{(E_1 + E_2)^2 - (\mathbf{p}_1 + \mathbf{p}_2)^2} \tag{3.1}$$

The Mandelstam variable s is a Lorentz-invariant quantity defined as the squared sum of the four-momenta of the initial-state particles. E_{CM} is often identified as $\sqrt{s}$, which is explained in the following equation:

$$\begin{aligned} s &= (p_1 + p_2)^2 \\ &= p_1^2 + p_2^2 + 2p_1 \cdot p_2 \\ &= (E_1^2 - \mathbf{p}_1^2) + (E_2^2 - \mathbf{p}_2^2) + 2(E_1 E_2 - \mathbf{p}_1 \cdot \mathbf{p}_2) \\ &= (E_1 + E_2)^2 - (\mathbf{p}_1 + \mathbf{p}_2)^2 \\ &= E_{\mathrm{CM}}^2 \end{aligned} \tag{3.2}$$

From these expressions, it can be shown that in fixed-target experiments, the centre-of-mass energy varies as the square-root of the beam energy (which is the energy of the incident particle, here, assumed to be E_1) as given in Equation 3.3

$$E_{CM} \approx \sqrt{2m_2E_1} \qquad : \text{for fixed-target experiments} \tag{3.3}$$

whereas in (symmetric) collider experiments, the centre-of-mass energy varies as twice the beam energy (which is the energy of either particle since $E_1 = E_2$ and is denoted here as E) as given in Equation 3.4.

$$E_{CM} \approx 2E \qquad : \text{for collider experiments} \tag{3.4}$$

Therefore, collider experiments like the LHC are favoured for particle production at high energies. Besides the centre-of-mass energy, other important quantities in such experiments are luminosity and cross-section. The cross-section σ of a process is given by

$$\sigma = \frac{\text{No. of interactions per unit time per target particle}}{\text{Incident flux}} \tag{3.5}$$

Theoretically, the cross-section of a process is a quantum mechanical probability for the process to occur computed from all the Feynman diagrams that contribute to the process. In collider physics, the cross-section is expressed as

$$\sigma = \frac{N}{\mathcal{L}_{\text{int}}} \quad , \tag{3.6}$$

where, N is the number of events of the process and $\mathcal{L}_{\text{int}}$ is the integrated luminosity which is calculated by summing over the instantaneous luminosity $\mathcal{L}$ over the operation lifetime of the machine, given by

$$\mathcal{L}_{\text{int}} = \int \mathcal{L}(t)\mathrm{d}t. \tag{3.7}$$

Particles in an accelerators are usually grouped into bunches that are collided at one or more interaction points where the various detectors are situated. The instantaneous luminosity (Equation 3.8) can be determined from the parameters of the colliding beams, namely, the number of particles in the colliding bunches, denoted as n_1 and n_2, the frequency of the bunch collisions, f and the RMS (root mean square) values of the beam sizes, σ_x and σ_y, assumed to have Gaussian profiles undergoing head-on collisions.

$$\mathcal{L} = \frac{f n_1 n_2}{4\pi\sigma_x\sigma_y} \tag{3.8}$$

The colliding beams produce many interactions and each individual interaction is termed as an *event*. Technologically advanced detector systems are employed to measure the properties of the numerous particles that are produced in the interactions in order to be able to identify them. A transverse cut-out of the ATLAS detector system is illustrated in Figure 3.1 which are described in detail in Section 3.3.

Tracking systems reconstruct the tracks of charged particles and help determine their electric charge and momenta from the curvature of the tracks. Powerful magnet systems enable such curvatures to form using the principle of Lorentz force where a magnetic field deflects the path of a charged particle in a direction dependent on the sign of the charge. Energy deposits of particles from the calorimeters

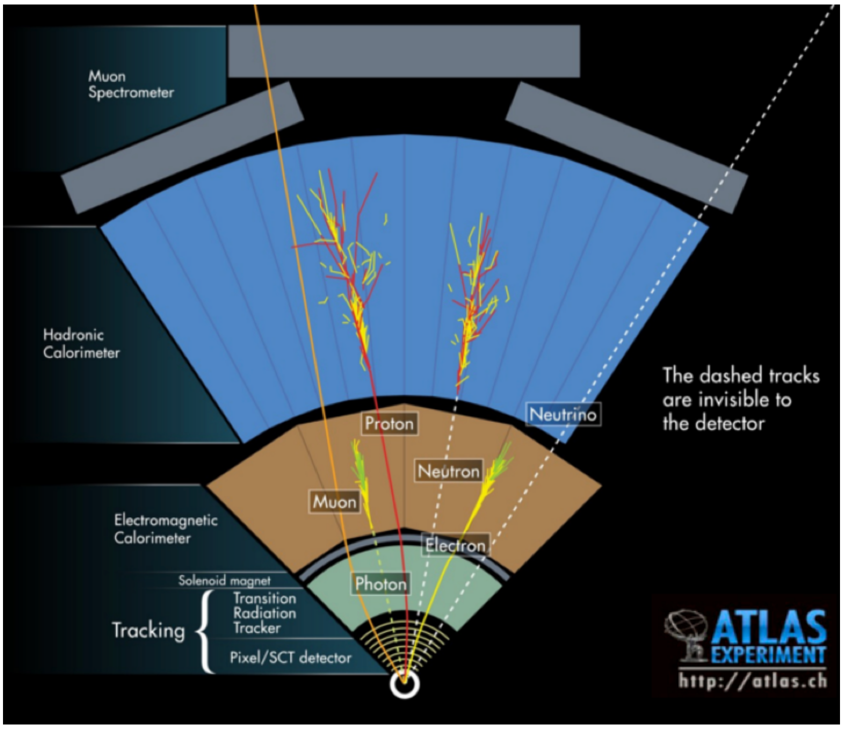

Figure 3.1: Transverse cut-out of the ATLAS detector system illustrating the signatures of different particles. The ATLAS Experiment © CERN

are used for their identification. Neutrinos remain undetected and their presence can deduced from the *missing momentum* which is the negative sum of momenta of all the observed particles in an event. Quarks are not observed as independent particles as they combine with other quarks to form hadrons. The energy in the strong interaction field between two quarks flying at relativistic velocities gives rise to another pair of quarks and anti-quarks and this process leads to the formation of a *jet*-like structure of hadrons. Of these, hadrons formed of b-quarks are relatively long-lived ($\tau \approx 1.5 \times 10^{-12}$ s) and, due to their Lorentz boost ($\beta\gamma$), travel a few millimeters before they decay. Consequently, as illustrated in Figure 3.2, the b-quark has a distinct signature of a jet of particles emanating from the collision point (primary vertex) and a displaced secondary vertex where the b-decay takes place.

3.2 The Large Hadron Collider

The Large Hadron Collider is a circular particle accelerator which lies within a tunnel of circumference of 26.7 km at a depth ranging between 50 and 175 m beneath the Franco-Swiss border near Geneva. The collider tunnel consists of two beam pipes kept at ultrahigh vacuum and ultracold temperatures in which proton beams are made to travel nearly at the speed of light in opposite directions with the help strong magnetic fields generated by superconducting magnets. The beam pipes intersect at four points inside the tunnel where the particle collisions take place and are detected by the ATLAS, CMS, ALICE and LHCb detectors. ATLAS and CMS are large general-purpose detectors, ALICE aims at studying heavy-ion collisions and the resultant quark-gluon plasma and LHCb focusses on decays

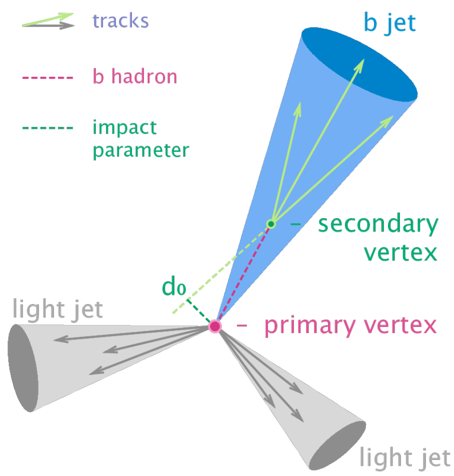

Figure 3.2: Illustration of b-tagging taken from [25]

of B-particles and the phenomenon of CP-violation. TOTEM, LHCf and MoEDAL are three other smaller detectors sharing caverns with one of the four mentioned earlier and have very specialized research aims. Figure 3.3 gives a schematic of CERN's accelerator complex. The LHC is operated to collide bunches of 10^{11} protons with a spacing of 25 ns at a centre-of-mass energy of 13 TeV with a design instantaneous luminosity of $10^{34}\,\mathrm{cm}^{-2}\mathrm{s}^{-1}$. The first data-taking period of the LHC, also called Run 1, started in 2009 and lasted for four years during which the energy was boosted from 900 GeV up to 8 TeV and in 2012, it reached a peak instantaneous luminosity of $7.7 \times 10^{33}\,\mathrm{cm}^{-2}\mathrm{s}^{-1}$, close to the design luminosity [26]. This Run was very successful; it resulted in about $30\,\mathrm{fb}^{-1}$ of proton data and important physics results, most notably the discovery of the Higgs boson [27, 28]. After a long shutdown during which various upgrades were made to prepare the collider for higher luminosities and an amplified centre-of-mass energy of 13 TeV, Run 2 began in 2015, during which a peak luminosity of $1.37 \times 10^{34}\,\mathrm{cm}^{-2}\mathrm{s}^{-1}$, higher than the LHC design value, has already been achieved. The total integrated luminosity over the period 2015-2017 is shown in Figure 3.4.

3.3 The ATLAS Detector

The ATLAS detector [31] is a general-purpose detector designed to accommodate a wide range of studies that answer questions on the fundamental building blocks matter, the forces that govern their interactions and beyond. The detector structure is 46 m long, 25 m high and weighs nearly 7000 tons. The ATLAS detector consists of a series of ever-larger concentric cylinders around the interaction point where the proton beams from the LHC collide. The four major subsystems of the detector – the Inner Detector (ID), the calorimeters, the Muon Spectrometer and the magnet systems – are described in the following subsections and illustrated in Figure 3.5. However, it is useful to precede them with a brief description of the ATLAS coordinate system, that will be used throughout this thesis.

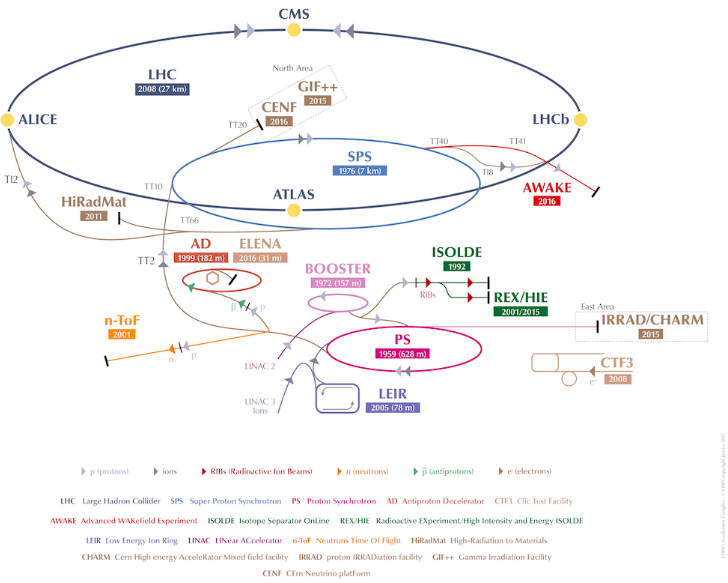

Figure 3.3: The LHC is the last ring (dark blue line) in a complex chain of particle accelerators. The smaller machines are used in a chain to help boost the particles to their final energies and provide beams to a whole set of smaller experiments, which also aim to uncover the mysteries of the Universe. [29] © CERN

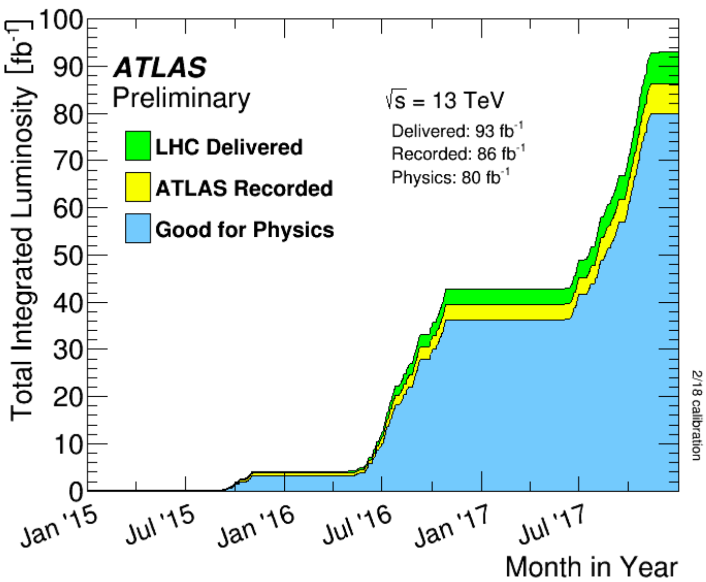

Figure 3.4: Total integrated luminosity delivered by the LHC 2015-2017 [30]. Data used in this thesis corresponds to the years 2015 and 2016 and amounts to 36.1 fb^{-1}.

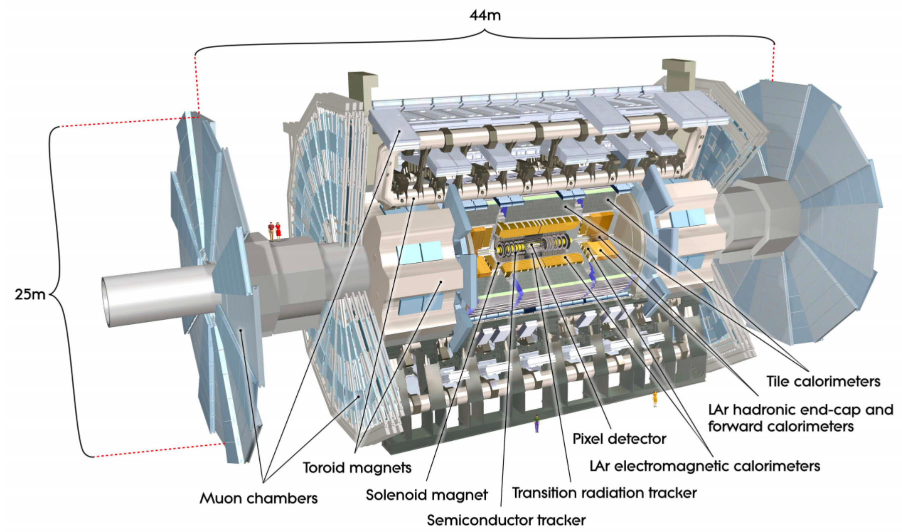

Figure 3.5: Cut-away view of the ATLAS detector [31]

3.3.1 The ATLAS Coordinate System

The origin of this coordinate system is positioned at the expected point of interaction. The positive x-axis is directed to the centre of the LHC ring from the point of interaction and the positive y-axis is directed upwards. The positive z-axis is chosen such that it results in a right-handed coordinate system. The transverse plane is the one perpendicular to the beam axis, containing the x and y axes. The transverse momentum, p_T, of a particle is an important kinematical quantity as, unlike the longitudnal momentum (which could arise from particles moving in the direction of the beam), it is associated with the physics processes that occurred at the point of interaction. It is defined as

$$p_T = \sqrt{p_x^2 + p_y^2}. \tag{3.9}$$

The azimuthal angle (ϕ) is measured from the positive x-axis to the projection of an arbitrary direction on the transverse plane. The polar angle (θ) is the angle from the positive z-axis to the arbitrary direction. A quantity more useful than the polar angle due to its Lorentz-invariance under longitudnal boosts is called pseudorapidity (η) and is defined as

$$\eta = -\ln\tan(\theta/2). \tag{3.10}$$

The distance between particles or jets can be expressed as the angular separation (ΔR) which is defined in the (η,ϕ)-plane as

$$\Delta R = \sqrt{\Delta\phi^2 + \Delta\eta^2}. \tag{3.11}$$

Quantities defined in the transverse plane are transverse energy E_T, transverse momentum p_T and missing transverse energy E_T^{miss}.

3.3.2 Inner Detector

The ATLAS Inner Detector (ID) measures the direction, momentum and charge of electrically-charged particles produced in each proton-proton collision. It is designed to generate high-quality momentum resolution, pattern recognition and both primary and secondary vertex measurements for charged tracks above a given p_T threshold and within the pseudorapidity range $|\eta| < 2.5$. The ID consists of three parts

- Pixel Detector
- Semiconductor Tracker
- Transition Radiation Tracker

all of which are traversed by a 2 T magnetic field parallel to the beam axis. Pixel and silicon micro-strip trackers, used in conjunction with the straw tubes of the Transition Radiation Tracker, possess very fine detector granularity to produce the high-precision measurements that are necessary for the momentum and vertex resolution. The precision tracking detectors (pixels and SCT) cover the region $|\eta| < 2.5$. In the barrel region, they are arranged on concentric cylinders around the beam axis while in the end-cap regions they are located on disks perpendicular to the beam axis.

During the upgrades that were made for Run 2, a fourth pixel layer, the insertable B-layer (IBL) [32], was added to achieve improved track and vertex reconstruction performance at higher luminosities. Significant improvements in the impact parameter resolution and primary vertex reconstruction led to improved b-tagging performances, in the low and medium jet-p_T regions [33].

3.3.3 Calorimeter

Calorimeters are designed to measure the energy that a particle (charged or neutral) loses as it passes through the material of the calorimeter. As a sufficiently long-lived particle passes through the material of the calorimeter, it undergoes interaction with the atoms and nuclei of the material, thereby generating particle showers and eventually depositing all of its energy. The ATLAS calorimetry consists of electromagnetic calorimeters (ECALs) and hadronic calorimeters (HCALs) covering the rapidity region up to $|\eta| < 4.9$.

ECAL They are used to measure the energy of electrons and photons through their electromagnetic interactions with the material of the calorimeter. The ATLAS ECAL is an accordian-shaped sampling calorimeter with Liquid argon (LAr) as its active material and lead as the absorber which covers the pseudorapidity region $|\eta| < 3.2$. The forward region ($3.1 < |\eta| < 4.9$) comprises copper/LAr calorimeters.

HCAL They are used to measure the energy of hadrons via their strong and electromagnetic interactions. The ATLAS HCAL is located outside the solenoid coil and the ECAL. In the range $|\eta| < 1.6$, it consists of scintillating tiles interleaved with iron absorbers. LAr sampling calorimetery with copper-plates as absorbers is used in the end-caps covering $1.5|\eta| < 3.2$. The forward region ($3.1 < |\eta| < 4.9$) comprises tungsten/LAr calorimeters.

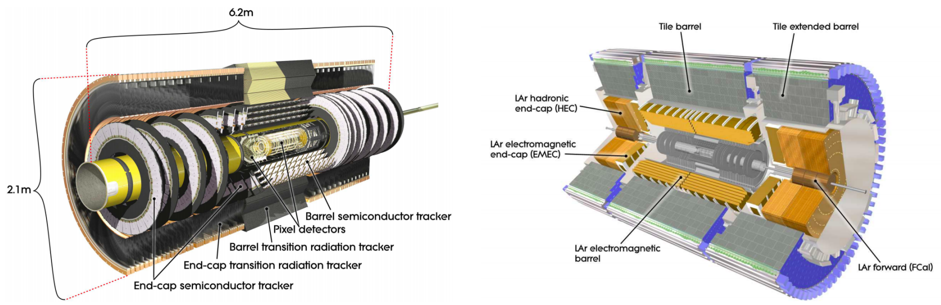

(a) (b)

Figure 3.6: Cut-away views of (a) the ATLAS Inner Detector and (b) the calorimeter system [31].

3.3.4 Muon Spectrometer

Muons, being much heavier leptons than electrons, do not lose all of their energy in the calorimeters. Consequently, a separate muon detection and trigger system, called the Muon Spectrometer, forms the outermost layer of the ATLAS detection system, which detects and measures the momentum of charged particles that pass through the barrel and end-cap calorimeters within the pseudorapidity range of $|\eta| < 2.7$. Magnetic fields are generated by a large barrel toroid in the $|\eta| < 1.4$ region, by two smaller end-cap magnets in the $1.6 < |\eta| < 2.7$ region and by a combination of barrel and end-cap magnets in the transition region $1.4 < |\eta| < 1.6$ [31]. Different kinds of muon chambers are present in cylindrical layers (in the barrel region) and in transverse planes (in the end-cap region) to give precise measurements of the tracks.

3.3.5 Magnet System

Particle trajectories are bent by fields generated by the magnetic system in the different layers of the detectors. The ATLAS magnet system comprises four large superconducting magnets which are very briefly discussed here:

- a central solenoid magnet, which produces a 2 T axial magnetic field for ID and is aligned on the beam axis
- a barrel toroid and two end-cap toroids, which produce a toroidal magnetic field of ≈ 0.5 T and 1 T for the muon detectors in the central and end-cap regions, respectively.

3.3.6 Trigger and Data Acquisition System

The huge number of proton-proton collisions that take place in and are detected by ATLAS can amount to millions of megabytes of data in a second. The fact that not all of these collisions provide interesting physics information makes it essential to have a trigger system in place to moderate the data flow and retain only those events that could be useful for physics analyses. To accomplish this, the ATLAS Trigger and Data Acquisition (TDAQ) system has been implemented to manage the sub-detectors readout and the event selection, thereby generating usable datasets.

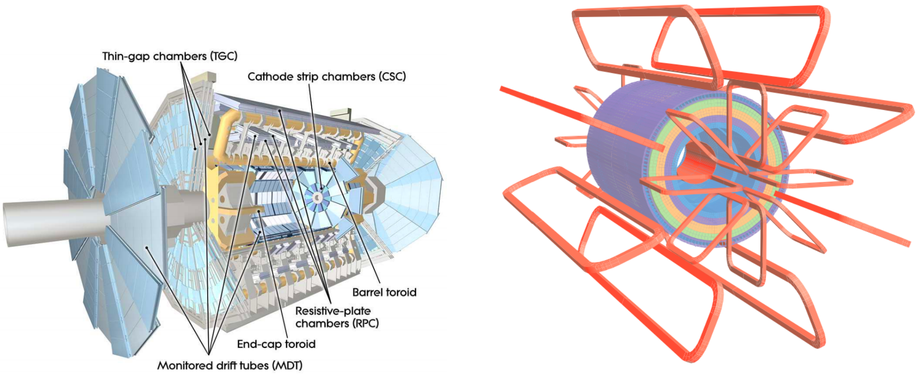

(a) (b)

Figure 3.7: Cut-away views of (a) the ATLAS muon system and (b) the magnet system [31].

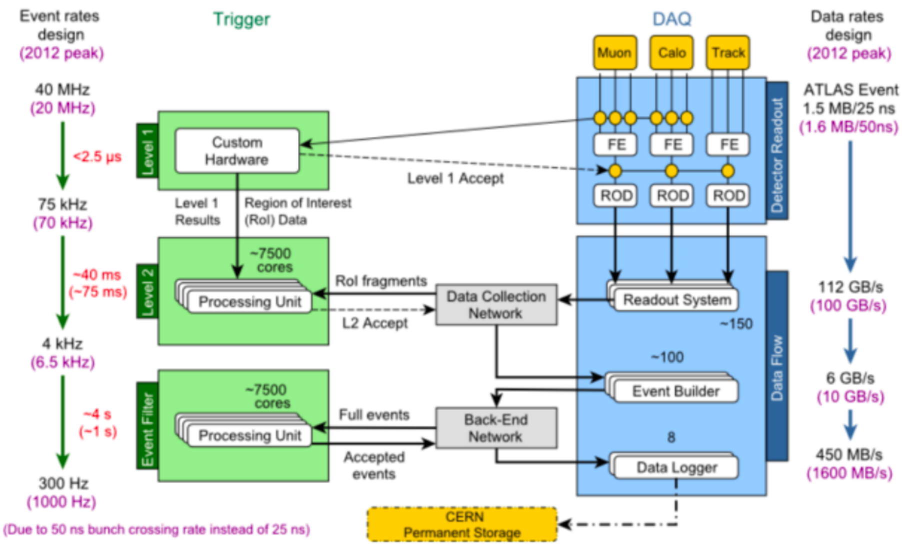

Figure 3.8: The ATLAS DAQ System in LHC Run 1 [34]

The trigger system consists of three levels: Level-1 (L1), Level-2 (L2) and the Event Filter (EF) of which L1 is based on customized hardware, and L2 and EF, collectively called the High-Level Trigger (HLT) are software triggers. The Data AcQuisition (DAQ) system collects the data from the different parts of the detector, converts the data in a suitable format and saves it to permanent storage.

A subset of information from the calorimeters and muon detectors are then handled by the Level-1 (L1) trigger which makes decisions with a latency of 2.5 μs of either rejecting or further processing an event. Data associated with an event that has been selected by the L1 trigger are then read from all detector components and are transmitted via optical fibres from readout drivers (RODs) to the readout system (ROS), which is the first part of the DAQ system. Less than a hundred thousand bunch crossings out of 40 million are retained by the L1 trigger. Further event selection is performed after constructing regions of interest (ROIs) depending on the location in the detector where interesting signals were found, which are then processed by the Level-2 (L2) trigger. Events that pass through L2 are subsequently sent to the EF, which is a large farm of CPUs that perform a detailed analysis of the fully-built events. L3 passes on upto 1000 events per second to a data storage system for offline analysis. The readout system is the first stage of data acquisition where local buffers receive and temporarily store data that are selected by the L1 trigger. After further selections from the HLT, data are transferred to permanent storage systems at CERN.

The design of the ATLAS TDAQ system for Run 1 is shown in Figure 3.8. References [31], [35], [34] and [36] give detailed descriptions of the systems, their performances and upgrades.

CHAPTER 4

Analysis Setup

This chapter is aimed at motivating the search and reporting the current status of cLFV in top-quark decays. It is followed by a description of the simulations for the signal and background processes, and the datasets, physics objects and other event selection aspects that were used for this analysis. Section 4.1 introduces the signal that is studied and Section 4.2 describes the Monte Carlo (MC)-simulated signal and background processes. Section 4.3 gives an account of the physics objects identified and reconstructed and Section 4.4 outlines the selection criteria placed on events to ensure that the datasets contain physics information relevant to the analysis.

4.1 The Signal Process

In this analysis, a search for cLFV is made in the decay $t(\bar{t}) \rightarrow \ell^{\pm}\ell'^{\mp}q(\overline{q})$, where $q \in u, c$ and $\ell \in \mu, \tau$ in $t\bar{t}$ events, where the other top-quark of the pair decays according to the SM into a b-quark and a leptonically-decaying W-boson as shown in Figure 4.1.

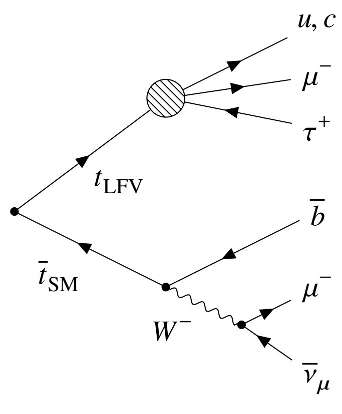

Figure 4.1: Example Feynman diagram for the process under study. [3]

The decay under study is expressed in terms of dimension six EFT operators and the current bounds on the coefficients of these operators are presented in Reference [18] which are derived from rare meson decays and single-top searches at the HERA (Hadron-Electron Ring Accelerator) experiment. The coefficients that involve a muon and a τ-lepton are relatively loosely constrained – ranging between

0.8 and 100 for axial-vector operators and from 0.03 to 100 for scalar and pseudo-scalar operators. However, the bounds on the operator coefficients are strongly dependent on the flavour composition of the leptons (especially on the presence of a τ-lepton).

A first dedicated search for cLFV has been performed in the the channel $t \to \ell^{\pm}\ell'^{\mp}q(\overline{q})$, where $q \in u, c$ and $\ell \in e, \mu, \tau$ in Reference [2] using $t\bar{t}$ events at the ATLAS experiment. It sets an upper limit on the branching ratio of the decay $t \to \ell\ell' q$ of 1.86×10^{-5} at 95% confidence level. In addiditon, it focusses on the channel where $\ell \in e, \mu$, discarding the τ from the cLFV vertex, and sets an upper bound on the branching ratio of this decay channel at 6.6×10^{-6}. The work of this thesis, instead, focusses on the $\mu - \tau$ final state and complements the picture of a first direct search for cLFV in top-quark decays.

4.2 MC Simulation of Signal and Background

4.2.1 Signal

The signal process simulated for this analysis is $t\bar{t} \to (\mu\tau q)((W \to \mu\nu)b)$. The sample was simulated by the MadGraph2.4.5 generator for the hard process and by Pythia 8 [37] for the showering and hadronisation. Geant 4 [38] was used to simulate the interactions of the particles with the ATLAS detector system. The nominal cross-section of the signal process σ_{LFV} is determined by using Equation 4.1

$$\sigma_{\text{LFV}} = \sigma_{t\bar{t}} \times 2 \times \text{BR}(t_{\text{LFV}}) \times \text{BR}(t_{\text{SM,lep}}) \tag{4.1}$$

where $\sigma_{t\bar{t}} = 831.76\,\text{pb}$ [39, 40] is the production cross-section of a top-antitop quark pair calculated at next-to-net leading order, including next-to-next leading logarithm resummation, the factor 2 is due to the interchangeability of the top quarks, $\text{BR}(t_{\text{LFV}})$ is the branching ratio of the top decaying via the lepton-flavour violating mode into a μ, τ and a light quark, is set to 10^{-4}, where the power of ten is arbitrary so that the value is comparable to those used in [18] and $\text{BR}(t_{\text{SM,lep}}) \approx 0.33$ [22] is the branching ratio of the other top. Inserting these values, we obtain $\sigma_{\text{LFV}} = 54.90\,\text{fb}$. The τ is allowed to decay via any mode in the signal sample and in the calculation of the cross-section.

4.2.2 Background Processes

The background samples that have been used in this analysis, along with the event generators and parton-shower generators, are listed in Table 4.1 and the list of individual datasets processed are given in Appendix A. These are processes that mimic the signature of the signal and as such, generally contain at least two jets, at least two leptons and missing energy in their final states. Processes that contain less than two leptons or jets in their final states can still serve as background because of their high cross-section. An additional lepton can be present due to mis-identification of particles or non-prompt sources like decay of hadrons and photon conversion. An additional jet can be present due to QCD radiation of gluons.

Diboson Grouped according to their final states instead of the boson involved, the diboson processes are included in the $\boldsymbol{4\ell}$, $\boldsymbol{3\ell\nu}$ and $\boldsymbol{\ell\nu qq}$ samples which are mainly the ZZ, WZ and a combination of the WW and WZ production channels.

$t\bar{t}$ and $t\bar{t}\gamma$ The $t\bar{t}$ production process has a relatively high cross-section and plays an important role later in the analysis as a source of leptons originating in non-prompt processes. The $t\bar{t}$ sample used in this analysis includes the dileptonic and lepton+jets decay channels of the top quarks. A photon can also be emitted by initial or final state particles which can then undergo photon-conversion or be mis-identified as an electron. It is accounted for in the $t\bar{t}$ sample at the parton-shower generation step and included in the matrix element itself in a separate $t\bar{t}\gamma$ sample. The resultant possible overlap between the two samples is removed using generator information.

$t\bar{t}H$, $t\bar{t}W$ and $t\bar{t}Z$ The associated production of $t\bar{t}$ along with vector ($t\bar{t}W$ and $t\bar{t}Z$) and scalar ($t\bar{t}H$) bosons are included as background owing to the production of three or more prompt leptons and additional jets.

Single top The $t + X$ sample comprises the production of a single top quark in association with a vector boson, namely the tZ and tW samples. The tWZ process is also included in the background.

W + jets The production of the W boson with additional jets also contributes to the background even though its final state comprises only one lepton. Its high cross-section and the possibility of a lepton originating from a non-prompt source or a jet being mis-identified as a tau can cause it to enter the dilepton selection.

Z + jets and Z + γ Similar to the $t\bar{t}$ sample, the Z + jets production sample also has a high-cross section. Here also, there is a separate $Z + \gamma$ sample wherein the photon emission is accounted for in the matrix element and the overlap between the two samples is again removed using truth records.

Triboson The VVV sample includes triboson processes where V represents either a W or a Z boson.

Others Included in this category are background processes like the diboson production with $2\ell 2q$ and $2\ell 2\nu$ final states, associated production of a Higgs boson with a W boson or a Z boson or with a pair of gluons, SM production of three or four top quarks and the $t\bar{t}W^+W^-$ process.

4.3 Object Definitions and Event Selection

4.3.1 Definitions of Objects

The physics objects used in this analysis are muons, tau-leptons, jets, b-jets and missing transverse momentum. The identification and reconstruction criteria for these objects are discussed in brief below.

Muons Reconstruction of muons is carried out by combining tracks from the ID and the muon spectrometer [41]. Isolated energy deposits in the calorimeters accordant with the passage of minimum-ionizing particles are also put together with tracks from the ID in the $|\eta| < 0.1$ region. Isolation variables, namely track isolation[1] and calorimetric isolation[2], are used to reduce the background from

[1] Track isolation, denoted by `ptvarcone30`, is defined as the sum of transverse momenta of the tracks within a cone of $\Delta R = \min(0.3, 10\,\text{GeV}/p_{\text{T}}(\mu))$.

[2] Calorimetric isolation, denoted as `topoetcone20`, is defined as the sum of transverse energies of calorimeter clusters within a cone of $\Delta R = 0.2$ of the muon candidate.

Process	Event Generator	Parton Shower
$\boldsymbol{4\ell}$	Sherpa	
$\boldsymbol{3\ell\nu}$	Sherpa	
$\boldsymbol{\ell\nu qq}$	Sherpa	
$\boldsymbol{t\bar{t}}$	Powheg	Pythia 8
$\boldsymbol{t\bar{t}\gamma}$	MadGraph	Pythia 8
$\boldsymbol{t\bar{t}H}$	aMC@NLO	Pythia 8
$\boldsymbol{t\bar{t}W}$	aMC@NLO	Pythia 8
$\boldsymbol{t\bar{t}Z}$	aMC@NLO	Pythia 8
$\boldsymbol{W}$ **+ jets**	Sherpa	
$\boldsymbol{Z}$ **+ jets**	Sherpa	
$\boldsymbol{Z+\gamma}$	Sherpa	
VVV	Sherpa	
Single top:		
$t\ W$	aMC@NLO	Pythia 8
$t\ Z$	MadGraph	Pythia 6
$t\ W\ Z$	aMC@NLO	Pythia 8
Others:		
$2\ell 2q$	Sherpa	
$2\ell 2\nu$	Sherpa	
$2\ell 2\nu 2j$	Sherpa	
VH	Pythia 8	Pythia 8
$3t$	MadGraph	Pythia 8
$4t$	MadGraph	Pythia 8
$t\bar{t}W^+W^-$	MadGraph	Pythia 8

Table 4.1: Background processes simulated for the analysis and their event and parton shower generators

non-prompt muons originating in hadronic decays. The muons are classified as either *Tight* or *Loose*, where the *Tight* selection places restrictions[3] on the the muon isolation and the *Loose* selection places none. These selection criteria play an important role in the estimation of background from non-prompt muons and subsequently defining the Signal Region for the search in this analysis. Cuts made on the transverse and longitudinal impact parameters are $|d_0|/\sigma_{d_0} < 3$ and $|z_0 \sin(\theta)| < 0.5$ mm which ensure that muon candidates have originated at the primary vertex. Furthermore, muon candidates are also required to have $p_T > 10$ GeV and $|\eta| < 2.5$.

Electrons Reconstruction of electrons is performed by combining charged particle tracks in the ID that correspond to energy clusters in the ECAL [42]. Electron candidates are required to satisfy the conditions of $p_T > 10$ GeV and $|\eta_{clu}| < 2.47$ but are rejected if they fall in the calorimeter transition region $1.37 < |\eta_{clu}| < 1.52$. As in the case of muons, isolation variables are also used for electrons to diminish the non-prompt background from hadronic decays. The impact parameters are $|d_0|/\sigma_{d_0} < 5$

[3] The *Tight* muons are required to have track isolation `ptvarcone`$/p_T < 0.06$.

and $|z_0 \sin(\theta)| < 0.5$ mm.

Jets Reconstruction of jets [43] is done using three-dimensional topological clustering of individual calorimeter cell signals (TopoClusters) [44] using the anti-k_t algorithm [45] with a cone of $\Delta R = 0.4$. To eliminate jets that are produced from pile-up interactions with efficiencies independent of the primary vertex reconstruction, a requirement is placed on the Jet Vertex Tagger (JVT) discriminant [46] to be greater than 0.59 for jets with $p_T < 60$ GeV and $|\eta| < 2.5$. Candidate jets also need to satisfy the conditions of having $p_T > 25$ GeV and $|\eta| < 2.5$.

b-tagged Jets Jets that contain b-hadrons are called b-jets and are identified using the MV2c10 algorithm [47] where the 85% b-jet efficiency working point is chosen. The basic b-tagging algorithms used in ATLAS take information from tracks of charged particles from the ID. The best separation between jet-flavours is then provided by combining the outputs of these algorithms into a multivariate discriminant called MV2. Due to the high efficiency of selection (85%), the rejection rates for c-jets, other light-jets and τ-jets of this working point are low. However, this choice is justified by the statistically-challenged Signal Region of this analysis.

τ-leptons τ-leptons decay into hadrons roughly 65% of the time and tau-reconstruction [48] begins in manner similar to that of jets in the sense that a jet obtained using the anti-k_t algorithm with $\Delta R = 0.4$ and satisfying the conditions of $p_T > 25$ GeV and $|\eta| < 2.5$ is chosen as a seed for the τ_{had} reconstruction algorithm. The vertex location is computed by a tau vertex (TV) algorithm which sums the p_T of all candidate tau tracks in a region $\Delta R < 0.2$ and the candidate vertex which matches the highest p_T fraction is chosen. Further requirements are imposed for track selection. Typically, the jets formed by τ-decays are narrower and can leave either one or three tracks in the ID with a total charge of ± 1. Discriminating variables based on tracks and calorimetric clusters are used to reduce generic background from jets. The chosen working point has an efficiency of 55% (40%) for one-(three-)prong t_{had} decays.

Missing Transverse Momentum The missing transverse momentum vector p_T^{miss} is reconstructed [49] as the negative vector sum of the transverse momenta p_T of all detected particles, and its magnitude is denoted by E_T^{miss}. The energy scale and resolution of the reconstructed physics objects, viz., electrons, muons, τ-leptons and jets strongly affects the measurement of E_T^{miss}. Momentum contributions that do not originate from any of these physics objects are reconstructed as $(E_T^{miss})^{SoftTerm}$ and are also taken into account.

4.3.2 Overlap Removal (OLR)

There may exist an overlap of different identification categories for the same physics object e.g. a muon originating from the decay of hadrons within a jet can also be identified as an independent prompt muon. Such overlaps are eliminated by an OLR algorithm [50] which is performed on loose objects and the following rules are applied in the order specified below [51].

- Overlap between taus and electrons are removed by rejecting taus within $\Delta R < 0.2$ of a loose ID electron.
- Overlap between taus and muons is removed by rejecting τ-leptons which are within $\Delta R < 0.2$ of a loose muon. Taus are rejected if they are matched with a muon that satisfies $p_T > 2$ GeV

and, if the muon is combined[4] or the tau has $p_T > 50$ GeV.

- Overlap between electrons and muons is removed by rejecting calo-tagged muons that share an ID track with an electron and by rejecting electrons that share a track with the remaining muons.
- Overlap between jets and electrons is removed by rejecting jets within $\Delta R < 0.2$ of an electron and by rejecting electrons that are within $\Delta R < 0.4$ of remaining non-pileup[5] jets.
- Overlap between jets and muons is removed by rejecting jets that have less than three tracks and are either within $\Delta R < 0.2$ or ghost-matched [52] to a muon. Muons are rejected if they are within $\Delta R < 0.4$ of the remaining non-pileup jets.
- Overlap between jets and taus is removed by rejecting jets within $\Delta R < 0.4$ of a tau.

4.4 Event Selection

All the samples used in this analysis contain events with exactly two same-sign muons and a veto on electrons. The datasets used and further selections and triggers are reported in this section. They are followed by a description of the regions constructed for background validation and signal identification.

4.4.1 Data

The data used in this analysis are events recorded by the ATLAS detector during Run 2 of the LHC. The total integrated luminosity is 36.1 fb^{-1} taken from runs in 2015 (data periods D to J, amounting to 3.2 fb^{-1}) and in 2016 (data periods A to L, amounting to 32.9 fb^{-1}) at a centre-of-mass energy $\sqrt{s} = 13$ TeV and a bunch spacing of 25 ns.

4.4.2 Vertex Selection and Jet Cleaning

Vertex reconstruction makes use of track information from the ID to locate the points of primary interactions and secondary decays. It involves three major steps: a tight selection of tracks, seeding for the first vertex and estimation of the best vertex position with a fit [53]. The hard-scatter vertex is selected as the one with at least two tracks and with the highest $\sum p_T^2$, where the summation is made over all tracks with $p_T > 0.5$ GeV [54].

Events which contain at least one jet that originated from detector effects, beam background and cosmics are discarded using the JetCleaningTool [46] after the OLR procedure.

4.4.3 Triggers

Muons are triggered on by matching tracks reconstructed in the muon spectrometer and the ID. The muon triggers used in 2015 are:

- `HLT_mu20_iloose_L1MU15`
- `HLT_mu50`

[4] A muon is termed as "combined" when it has been reconstructed using tracks from the Muon Spectrometer and the ID.
[5] Pileup jets are those which have $p_T < 60$ GeV, $|\eta| < 2.4$ and JVT < 0.59.

and those used in 2016 are:

- `HLT_mu26_ivarmedium`
- `HLT_mu50`

Loose isolation requirements and a p_{T} threshold of 20 GeV were placed on the muons in 2015. In 2016, due to the higher instantaneous luminosity delivered by the LHC, the muons were required to pass tighter isolation criteria and a higher p_{T} threshold of 26 GeV. Moreover, muons with $p_{\mathrm{T}} > 50$ GeV were also selected without any isolation requirements in order to avoid efficiency losses due to isolation at high p_{T}.

CHAPTER 5

Analysis Strategy

The aim of this analysis is to search for the flavour-violating decay of the top quark to the μ-τ final state with one light quark, $t \rightarrow \mu^{\pm}\tau^{\mp}q$, in $t\bar{t}$ pair-production where the other top-quark decays according to the SM. A pre-selection region, defined to loosely match the signal signature, is introduced. Here the kinematic reconstruction is performed and the resulting variables are used to define a signal region. The background is estimated using simulated events and cross-checked with a data-driven technique. The number of expected and observed events in the signal region are then provided as input to a profile likelihood fit in order to test the presence of a signal.

Section 5.1 defines the regions used in the analysis, Section 5.2 describes the kinematic reconstruction procedure, while Section 5.3 is dedicated to the data-driven non-prompt muon background estimation. A short Section 5.4 presents a brief discussion on fake τ-leptons.

5.1 Definitions of Regions

A Validation Region, a Pre-Selection Region and a Signal Region are designed and are described below. Following are the selections common to all the regions:

- The leading muon is required to have $p_{\mathrm{T}} > 27\,\mathrm{GeV}$.
- Events should have at least one trigger-matched muon and at least one τ-lepton.

Validation Region A Validation Region is defined to legitimize the MC simulation of the background processes. For this purpose, a signal-depleted region is designed by having the jet multiplicity reduced to less than two. Modelling of kinematic variables in the Validation Region is shown in Figure 5.1 and the yields are given in Table 5.1. It is evident from these plots that the MC simulation does not describe the data satisfactorily in this region which has a signal-to-background ratio of less than 3% thereby motivating the need for an alternative method to estimate the background[1].

Pre-Selection Region A Pre-Selection Region is defined orthogonal to the Validation Region with a cut on the jet multiplicity which is required to be at least two. Coupled with the common selections on muons and τ-leptons mentioned above, this region loosely emulates the signature of the process

[1] "Background" here refers specifically to that originating from non-prompt muons, described in Section 5.3.

under study. It is used for carrying out the kinematic reconstruction (described in Section 5.2) and the resulting variables are used to define a Signal Region. The signal and background yields are reported in Table 5.2 and Figure 5.2 shows the reconstructed kinematic variables in this region.

Signal Region The Signal Region is defined by enforcing narrower criteria on the Pre-Selection Region. The b-jet multiplicity has to be exactly one and both muons are constrained to be *tight*. The reconstructed invariant mass of the top quark that undergoes flavour-violating decay is required to be between 150 and 190 GeV. The yields for this region are reported in Table 5.3 and Figure 5.3 shows some kinematic distributions and reconstructed variables of this region with data blinded at this stage to eliminate experimental bias. It is in this region that the final fit procedure is carried out to test the presence of a signal in Section 6.2.

Sample	Raw	Yield
$3\ell\nu$	3150	31.7 ± 1.7
4ℓ	1709	4.98 ± 0.64
Others	206	5.0 ± 1.2
$t\bar{t}$	487	123.1 ± 7.0
$t\bar{t}H$	312	0.12 ± 0.03
$t\bar{t}W$	187	0.44 ± 0.06
$t\bar{t}Z$	88	0.16 ± 0.03
VVV	449	0.85 ± 0.07
Z + jets	191	20.7 ± 7.6
$t + X$	80	10.6 ± 1.8
$t\bar{t}\gamma$	36	1.44 ± 0.25
W + jets	187	31 ± 14
$\ell\nu qq$	13	2.3 ± 1.5
Total Bkg.	7129	232 ± 18
Signal	1725	6.82 ± 0.28
S/B		(2.93 ± 0.26)%
Data	289	289
Data/MC		1.24

Table 5.1: MC raw events, yields and data in the Validation Region.

5.2 Kinematic Reconstruction

The two top-quarks of the signal are reconstructed in the Pre-Selection Region from their decay products. The one that undergoes a flavour-violating decay is labelled as the *LFV top* and the one that decays leptonically in accordance with the Standard Model is labelled as the *SM top*.

LFV top For each event, the jet with the highest b-tag likelihood (which is given by the MV2c10 score) is reserved for the reconstruction of the SM top. Each of the remaining jets are combined

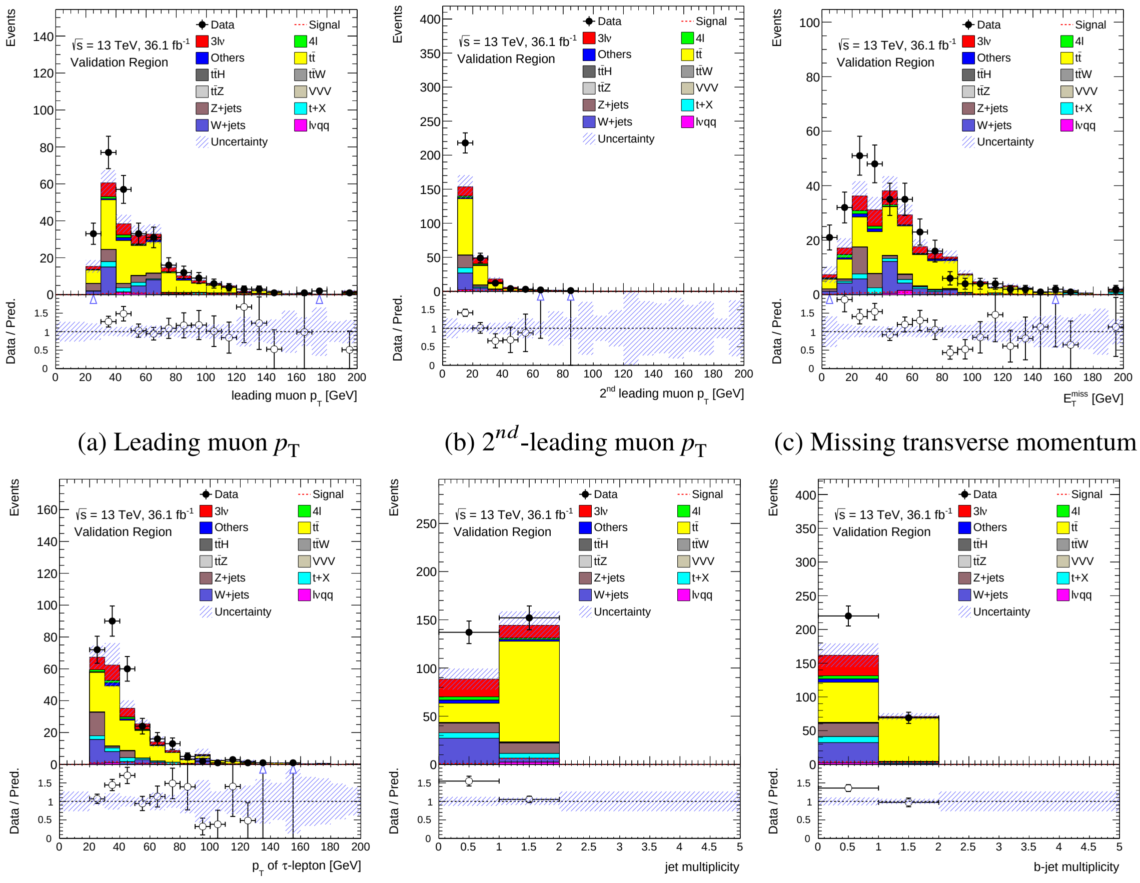

(a) Leading muon p_T (b) 2^{nd}-leading muon p_T (c) Missing transverse momentum

(d) τ-lepton p_T (e) Jet multiplicity (f) b-jet multiplicity

Figure 5.1: Kinematic distributions of MC vs. data in the Validation Region. Only statistical uncertainties are shown. Last bins of figures (a) and (c) contain overflow.

with a pair of opposite-sign different-flavour leptons, here, a muon and a tau-lepton of opposite signs, to give a set of candidates for the LFV top. The designated LFV top candidate is the one whose reconstructed invariant mass is closest to the mass of the top quark (172.5 GeV). The jet and leptons that have been employed in the LFV top reconstruction are excluded from subsequent steps of the SM top reconstruction.

SM top The previously reserved jet with the highest b-tag likelihood is combined with the remaining muon and the neutrino. The neutrino momentum reconstruction is executed in the following way:

The $E_\mathrm{T}^\mathrm{miss}$ variable gives information only about the x and y components of the neutrino momentum while the longitudinal component remains unknown. Adopting the idea presented in Ref. [55], the z-component of the neutrino momentum, $p_{z,\nu}$, is computed using Equation 5.1. Here, it has been assumed that the W boson is on-shell and has a pole mass $M_W = 80.4\,\mathrm{GeV}$. The derivation of this equation is given in Appendix B.

$$p_{z,\nu}^{\pm} = \frac{\mu p_{z,\ell}}{p_{\mathrm{T},\ell}^2} \pm \sqrt{\frac{\mu^2 p_{z,\ell}^2}{p_{\mathrm{T},\ell}^4} - \frac{E_\ell^2 p_{z,\ell}^2 - \mu^2}{p_{\mathrm{T},\ell}^2}} \qquad \text{where} \qquad \mu = \frac{M_W^2}{2} + p_{\mathrm{T},\ell} p_{\mathrm{T},\nu} \cos\Delta\phi \tag{5.1}$$

Here, ℓ in the subscripts represents a lepton, here a muon, $\Delta\phi$ is the azimuthal angle difference between the lepton and the $E_{\mathrm{T}}^{\mathrm{miss}}$. In the case that the discriminant of Equation 5.1 is positive, the solution with a smaller absolute value is chosen. However, the finite resolution of the $E_{\mathrm{T}}^{\mathrm{miss}}$ measurement or the possible existence of other neutrinos in the event can lead to negative values of the discriminant, resulting in complex solutions for $p_{z,\nu}$. A deeper analysis of the discriminant reveals that the case of complex solutions arises when the reconstructed transverse mass of the W boson, $M_{T,W}$, becomes larger than the pole mass, M_W as given in Equation 5.2.

$$M_W < M_{T,W} = \sqrt{2 p_{\mathrm{T},\ell} p_{\mathrm{T},\nu} (1 - \cos\Delta\phi)} \tag{5.2}$$

This situation is dealt with by minimally modifying the x and y components of $E_{\mathrm{T}}^{\mathrm{miss}}$ such that the solutions of Equation 5.1 become real. It is achieved by requiring $M_{T,W}$ to be exactly equal to M_W in Equation 5.2 which leads us to a quadratic relation between $p_{y,\nu}$ and $p_{x,\nu}$, the solutions to which are given in Equation 5.3.

$$p_{y,\nu}^{\pm}(p_{x,\nu}) = \frac{M_W^2 p_{y,\ell} + 2 p_{x,\ell} p_{y,\ell} p_{x,\nu}}{2 p_{x,\ell}^2} \pm \frac{M_W p_{\mathrm{T},\ell}}{2 p_{x,\ell}^2} \sqrt{M_W^2 + 4 p_{x,\ell} p_{x,\nu}} \tag{5.3}$$

The aim, then, is to minimize the difference between current transverse components of the neutrino momentum and the corresponding measured transverse components of $E_{\mathrm{T}}^{\mathrm{miss}}$ as given in Equation 5.4 to obtain unique values of the transverse components of the neutrino momentum.

$$\delta^{\pm}(p_{x,\nu}) = \sqrt{(p_{x,\nu} - E_{\mathrm{T},x}^{\mathrm{miss}})^2 + (p_{y,\nu}^{\pm}(p_{x,\nu}) - E_{\mathrm{T},y}^{\mathrm{miss}})^2} \tag{5.4}$$

The minimization is done in an iterative manner using the Brent method of one-dimensional minimisation, pre-defined in the ROOT data analysis framework [56]. Since $p_{y,\nu}$ is a function of $p_{x,\nu}$ as is evident from Equation 5.3, $p_{x,\nu}$ is therefore the only free minimization parameter which is constrained by the relation 5.5 to give only real solutions for $p_{y,\nu}$.

$$p_{x,\nu} \geq -\frac{M_W^2}{4 p_{x,\ell}} \tag{5.5}$$

Finally, the components of the neutrino momentum are given by the δ-minimizing $p_{x,\nu}$, its corresponding $p_{y,\nu}$, and $p_{z,\nu}$ given by Equation 5.1.

5.3 Data-Driven Estimation of Background

Non-prompt muons originate in semi-leptonic decays of bottom or charm mesons or from highly energetic hadronic showers that manage to pass through the hadronic calorimeter into the muon

Sample	Raw	Yield
$3\ell\nu$	2490	11.06 ± 0.48
4ℓ	940	1.05 ± 0.06
Others	310	1.56 ± 0.46
$t\bar{t}$	741	181.9 ± 6.9
$t\bar{t}H$	4625	3.41 ± 0.43
$t\bar{t}W$	1176	3.11 ± 0.15
$t\bar{t}Z$	1661	2.24 ± 0.15
VVV	217	0.33 ± 0.04
Z + jets	113	4.19 ± 1.7
$t + X$	160	7.7 ± 1.5
$t\bar{t}\gamma$	86	3.16 ± 0.35
W + jets	63	6.7 ± 1.1
$\ell\nu qq$	2	1.01 ± 0.94
Total Bkg.	12584	227.5 ± 7.5
Signal	6242	24.09 ± 0.31
S/B		(10.59 ± 2.60)%
Data	209	209

Table 5.2: MC raw events, yields and data in the Pre-Selection Region.

Sample	Raw	Yield
$3\ell\nu$	152	0.88 ± 0.24
4ℓ	62	0.07 ± 0.02
Others	20	0.10 ± 0.03
$t\bar{t}$	22	5.5 ± 1.2
$t\bar{t}H$	772	0.45 ± 0.03
$t\bar{t}W$	219	0.60 ± 0.06
$t\bar{t}Z$	315	0.45 ± 0.06
VVV	15	0.01 ± 0.00
Z + jets	3	0.15 ± 0.09
$t + X$	27	0.15 ± 0.05
$t\bar{t}\gamma$	5	0.16 ± 0.07
W + jets	2	0.17 ± 0.12
$\ell\nu qq$	0	0.00 ± 0.00
Total Bkg.	1614	8.69 ± 1.23
Signal	2241	8.52 ± 0.18
S/B		(98 ± 17)%

Table 5.3: MC raw events and yields in the Signal Region.

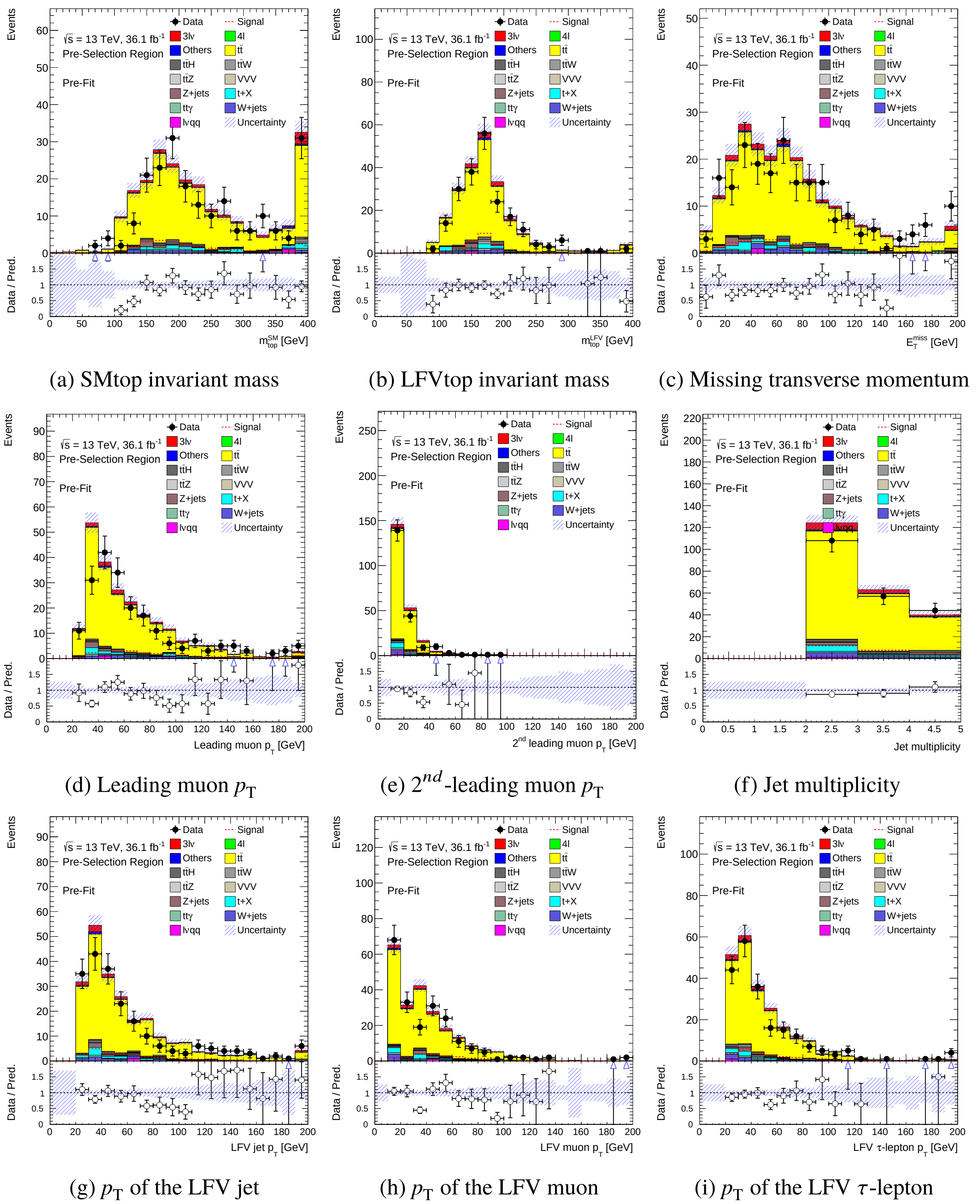

(a) SMtop invariant mass (b) LFVtop invariant mass (c) Missing transverse momentum

(d) Leading muon p_T (e) 2^{nd}-leading muon p_T (f) Jet multiplicity

(g) p_T of the LFV jet (h) p_T of the LFV muon (i) p_T of the LFV τ-lepton

Figure 5.2: Kinematic distributions and reconstructed variables in the Pre-Selection Region. Only statistical uncertainties are shown. Last bins of figures (a) and (c) contain overflow.

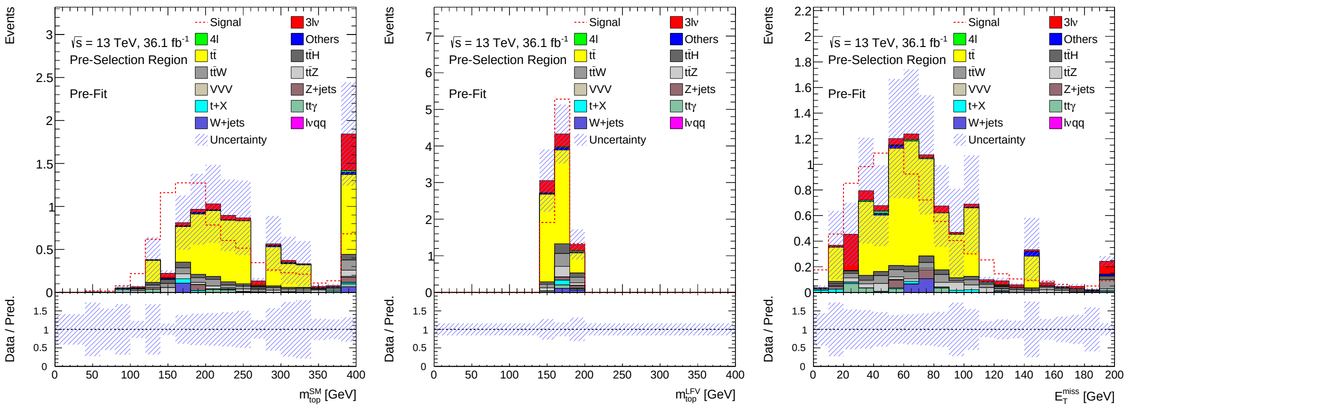

(a) SMtop invariant mass (b) LFVtop invariant mass (c) Missing transverse momentum

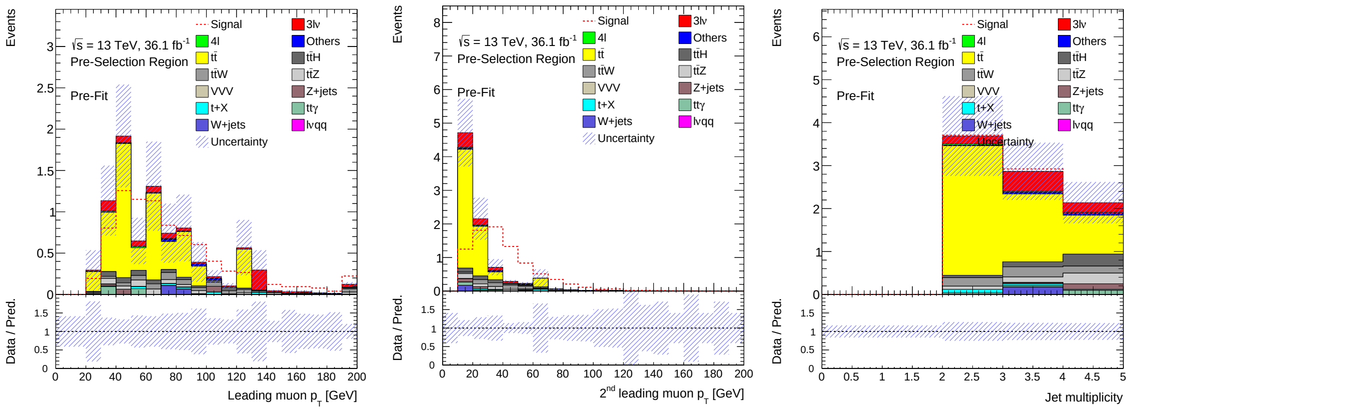

(d) Leading muon p_T (e) 2^{nd}-leading muon p_T (f) Jet multiplicity

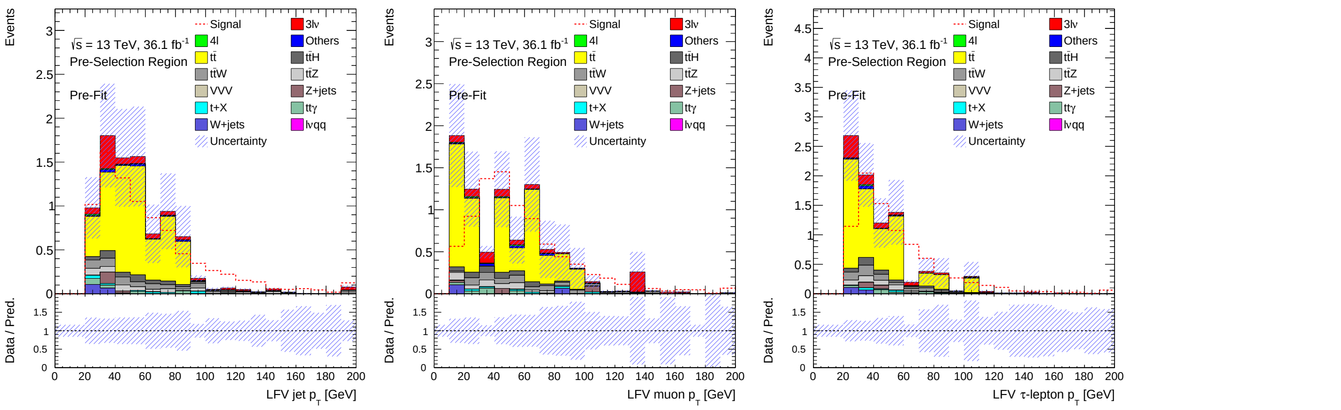

(g) p_T of the LFV jet (h) p_T of the LFV muon (i) p_T of the LFV τ-lepton

Figure 5.3: Kinematic distributions and reconstructed variables in the Signal Region. Data is blinded and only statistical uncertainties are shown. Last bins of figures (a) and (c) contain overflow.

detector system. Non-prompt τ-leptons arise mostly from jets that are misidentified as taus (Section 5.4).

The $t\bar{t}$ background process (Figure 5.4) necessarily has two opposite-sign leptons in its final state when decaying in the dilepton channel. Despite the requirement placed in the Pre-Selection Region to retain events with only same-sign muons, the $t\bar{t}$ process enters this selection due to the presence of an extra non-prompt muon that possibly originates in the decay of a b-hadron. Non-prompt background can be significant even in the presence of at least one non-prompt lepton as can be seen in the distributions of variables in the Pre-Selection Region (Figure 5.2) which is dominated by the $t\bar{t}$ background. Unfortunately, MC simulation is limited in its ability to predict background from non-prompt sources which leads to the necessity of utilizing data-driven methods. Nevertheless, such methods make use of the behaviour of non-prompt leptons with some help from MC simulations.

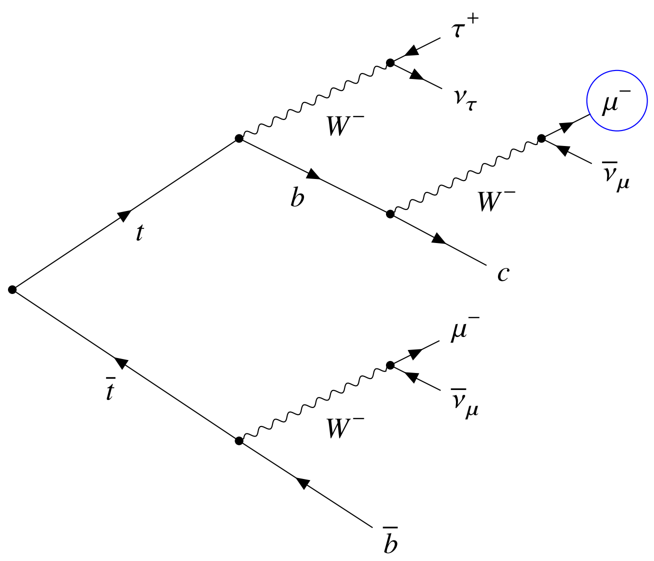

Figure 5.4: Example Feynman diagram for the $t\bar{t}$ background process which enters the same-sign muon selection due to the presence of an extra non-prompt muon (circled in blue). [3]

One such method is called the ABCD method [57] which has been deployed to estimate the non-prompt background from muons in the Signal Region. The method and its implementation strategy are described in the following subsections.

5.3.1 The ABCD Method

The ABCD method makes use of four mutually exclusive regions in phase space that are defined by making selections on two mutually independent variables that characterize the data in order to estimate the background (here, the estimation is made for background from non-prompt muon sources) in the signal-enriched region. The variables are chosen and the selections on them are made in a manner such that one of the regions is enriched in signal events while the remaining regions are not, while all of them are sufficiently evenly populated. A schematic for ease of visualization is given in Figure 5.5(a). Assuming a two-dimensional phase space spanned by two uncorrelated variables x and y, considering region D to be the signal-enriched region of interest and neglecting contribution from the signal in regions A and C, the background in D can estimated by the scaling the background in C by the ratio of those in B and A as given in Equation 5.6.

$$N_{\mathrm{D}} = \frac{N_{\mathrm{B}}}{N_{\mathrm{A}}} \times N_{\mathrm{C}} \tag{5.6}$$

where N_i is the number of background events from non-prompt muons in region i where $i \in \{A, B, C, D\}$. In this analysis, the four ABCD regions are defined in the Pre-Selection Region.

N.B.: N_i where $i \in \{A, B, C, D\}$ denotes the non-prompt contribution in region i and could have been best denoted as $N_i^{\text{non-prompt}}$. However, for the sake of clarity, the "non-prompt" superscript has been omitted. The reader is requested to not confuse it with total number of events.

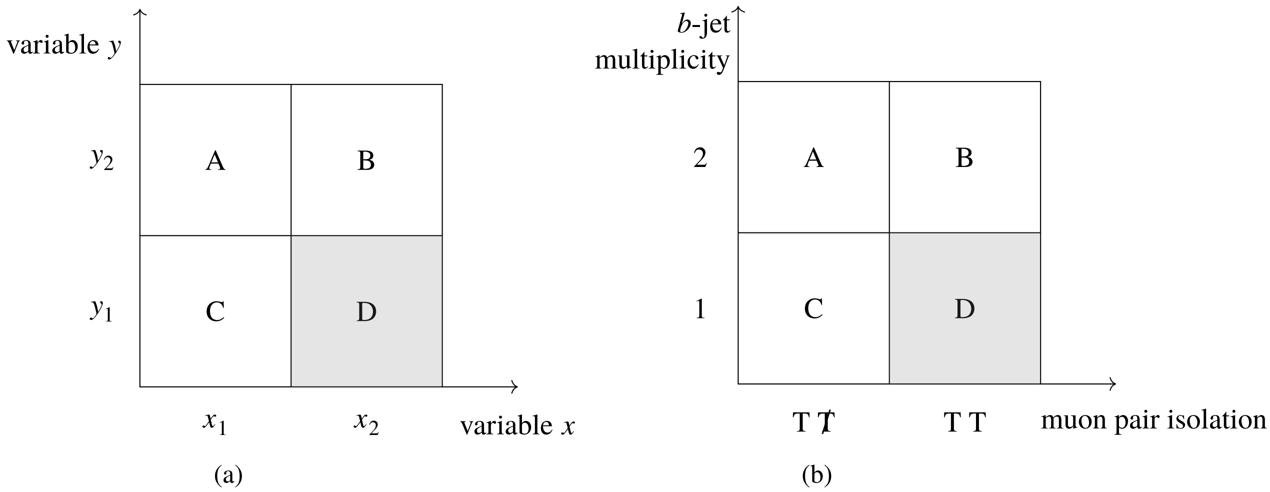

Figure 5.5: (a) Generic ABCD regions where x_i and y_i are the selections made on the variables x and y respectively. (b) ABCD regions as used in this analysis. Region D (in gray) is the signal-enriched region. For the muon pair isolation, T denotes the *tight* and $\not\mathrm{T}$ denotes the *anti-tight* definitions.

Choice of variables For a successful implementation of the ABCD method to estimate non-prompt background from data, it is of utmost importance to choose variables that ensure a dominance of non-prompt background in the control regions. In order to accomplish this, studies are made about the non-prompt muons' composition and their origins in the Pre-Selection Region. Referring to Figure 5.6 (and to Table 5.4 for an interpretation of the numbers), it is evident that the leading muon is very rarely non-prompt (approximately 11% of the time) whereas the sub-leading muon is almost always so (approximately 95% of the time). A major contribution to the non-prompt sub-leading muons comes from the $t\bar{t}$ sample. Referring to Figure 5.7, it can be seen that the leading muon is usually isolated while the sub-leading muon, non-isolated. The isolation parameter for the sub-leading muon allows the definition of control regions that are depleted in signal events. Consequently, it is used as one of the variables for the ABCD method.

The Pre-Selection Region has an overwhelming background from the $t\bar{t}$ sample which also turns out to be largest contributor to non-prompt muons. A selection placed on the number of b-tagged jets proves to be an effective way to have control regions that are sufficiently evenly populated with $t\bar{t}$ events.

Therefore, in Figure 5.5(b), the horizontal axis represents the muon pair isolation. The first T corresponds to the leading muon which is always *tight* in all regions. The second T corresponds to the sub-leading muon which is required to be *anti-tight*[2] in regions A and C and *tight* in regions B and D. The vertical axis represents the b-jet multiplicity. Events in regions A and B have two b-jets while those in regions C and D have one b-jet. Region D (in gray) is the Signal Region with both muons *tight* and one b-jet. Yields of all the individual background samples as well as the total background and signal content of the four regions A, B, C and D are reported in Table 5.5 where the dominance of the $t\bar{t}$ has been highlighted (in gray).

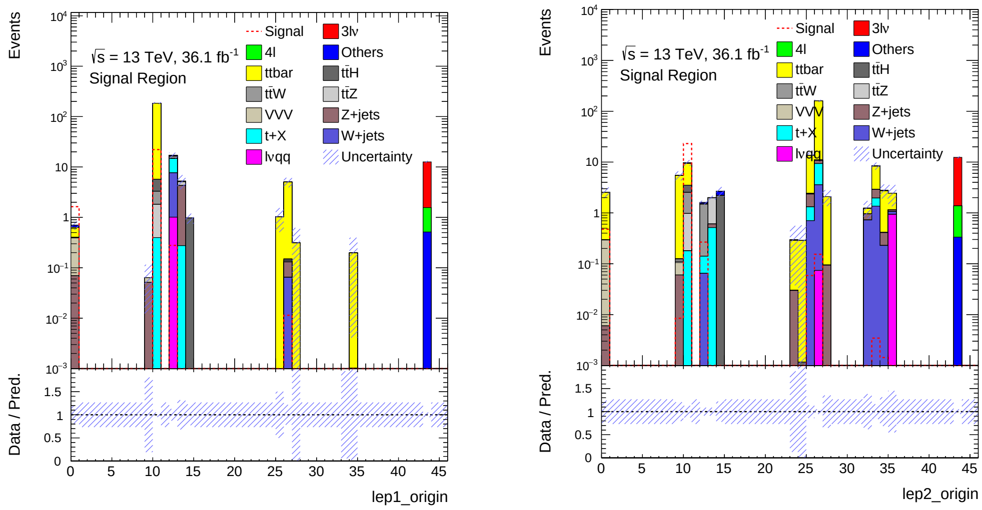

(a) Leading muon origin

(b) 2^{nd} leading muon origin

Figure 5.6: Origins of the (a) leading and (b) sub-leading muons. Interpretation of the numbers are given in Table 5.4. Note the log scale on the y-axis.

5.3.2 Closure Test

Before proceeding with the estimation of the non-prompt background on data, a preliminary check is carried out on MC simulation to validate the ABCD method. As was mentioned earlier, Table 5.5 shows the dominance of the $t\bar{t}$ background in all the regions. The method is applied *only* on this sample for a validation.

With D as the Signal Region in Equation 5.6, we use the ABCD method to obtain an expression for the expected number of non-prompt background events from MC simulation in region D, denoted by $N^{\text{MC}}_{\text{D,exp}}$ and given by Equation 5.7.

$$N^{\text{MC}}_{\text{D,exp}} = \frac{N^{\text{MC}}_{\text{B}}}{N^{\text{MC}}_{\text{A}}} \times N^{\text{MC}}_{\text{C}} \tag{5.7}$$

Using the MC yields of the $t\bar{t}$ sample in regions A, B and C from Table 5.5 for the right-hand side of Equation 5.7, we obtain $N^{\text{MC}}_{\text{D,exp}} = 29.0 \pm 8.7$ which is compatible with the actual MC yield of the $t\bar{t}$

[2] *Anti-tight* muons are those which do not satisfy the *tight* isolation requirements. They are not the same as *loose* muons.

Number	**Origin**
0	undefined
9	τ-lepton
10	t-quark
12	W-boson
13	Z-boson
14	Higgs
23	light-meson
24	s-meson
25	c-meson
26	b-meson
27	$c\bar{c}$ meson
32	c-baryon
33	b-baryon
34	π-decay
35	K-decay
43	diboson

Table 5.4: Muon origins. 10 and 12 correspond to prompt muons as they originate from a top-quark and a W-boson, respectively.

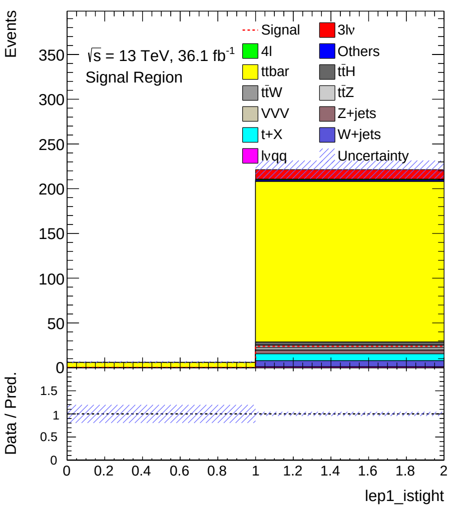

(a) Leading muon is *tight*

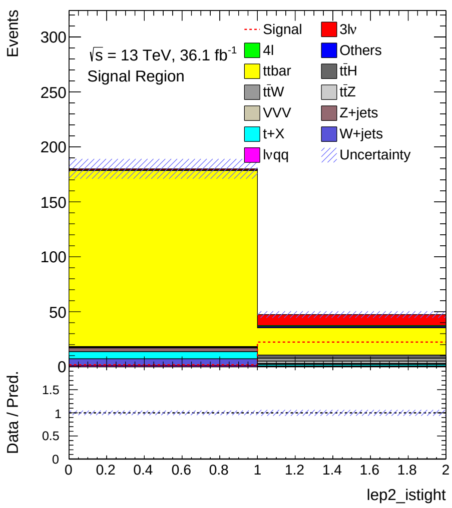

(b) 2$^{\text{nd}}$ leading muon is *tight*

Figure 5.7: The *tight* isolation criterion fulfilled by the (a) leading and (b) sub-leading muons. A value of zero denotes that the muon does not meet the condition and is *anti-tight* and a value of one denotes that it is *tight*.

sample in region D, $N_D^{\text{MC}} = 23.1 \pm 5.9$, within statistical uncertainty. The ABCD technique stands validated on MC and can be readily implemented on data.

Sample	**Region A**		**Region B**		**Region C**		**Region D**	
	Raw	Yield	Raw	Yield	Raw	Yield	Raw	Yield
$3\ell\nu$	5	0.02 ± 0.00	46	0.22 ± 0.00	51	0.42 ± 0.03	522	3.00 ± 0.12
4ℓ	5	0.00 ± 0.00	29	0.02 ± 0.00	31	0.04 ± 0.00	205	0.29 ± 0.00
Others	13	0.02 ± 0.00	61	0.11 ± 0.00	15	0.10 ± 0.00	47	0.33 ± 0.01
$t\bar{t}$	73	18.3 ± 5.0	14	3.27 ± 0.77	667	162 ± 42	94	23.1 ± 5.9
$t\bar{t}H$	353	0.20 ± 0.00	1824	1.21 ± 0.05	407	0.34 ± 0.01	1572	1.45 ± 0.13
$t\bar{t}W$	52	0.14 ± 0.00	477	1.31 ± 0.01	137	0.34 ± 0.00	587	1.53 ± 0.01
$t\bar{t}Z$	91	0.10 ± 0.00	629	0.89 ± 0.01	123	0.19 ± 0.00	675	0.92 ± 0.01
VVV	1	0.00 ± 0.00	6	0.01 ± 0.00	4	0.00 ± 0.00	66	0.09 ± 0.00
Z + jets	12	0.61 ± 0.06	1	0.00 ± 0.00	60	2.00 ± 2.62	15	-0.2 ± 1.5
$t + X$	8	0.57 ± 0.16	23	0.18 ± 0.00	26	3.68 ± 0.94	86	0.69 ± 0.13
$t\bar{t}\gamma$	17	0.54 ± 0.02	5	0.23 ± 0.01	55	2.10 ± 0.08	15	0.57 ± 0.02
W + jets	3	0.18 ± 0.01	1	0.10 ± 0.01	40	3.59 ± 0.68	7	0.80 ± 0.14
$\ell\nu qq$	0	0.00 ± 0.00	0	0.00 ± 0.00	0	0.00 ± 0.00	0	0.00 ± 0.00
Total Bkg.	633	20.6 ± 5.3	3116	7.56 ± 0.86	1616	175 ± 47	3892	32.6 ± 8.0
Signal	51	0.20 ± 0.00	935	3.55 ± 0.01	341	1.25 ± 0.00	4397	16.87 ± 0.07
S/B (%)		0.97 ± 0.25		47.0 ± 5.3		0.72 ± 0.19		52 ± 13

Table 5.5: Raw events and yields of background and signal samples in all the ABCD regions

5.3.3 Implementation on Data

Before using the ABCD formula on data for the estimation of non-prompt muon background in the signal region, a slight modification is made to Equation 5.6. Instead of directly using the data values of the control regions for N_{A}, N_{B} and N_{C}, the prompt contribution in the respective regions are subtracted from them, in order to ensure a dominance of non-prompt events, as is shown in Equation 5.8.

$$N_i = N_i^{\text{Data}} - N_i^{\text{prompt}}, \tag{5.8}$$

where N_i, as before, is the number of background events from non-prompt muons, N_i^{Data} is the number of data events and N_i^{prompt} are events with only prompt muons and $i \in \{A, B, C\}$. Finally, this leads us to Equation 5.9 which is used to make the estimation of background from non-prompt events in the signal-enriched region D, denoted by $N_{\text{D,exp}}$.

$$N_{\text{D,exp}} = \frac{\left(N_{\text{B}}^{\text{Data}} - N_{\text{B}}^{\text{prompt}}\right)}{\left(N_{\text{A}}^{\text{Data}} - N_{\text{A}}^{\text{prompt}}\right)} \times \left(N_{\text{C}}^{\text{Data}} - N_{\text{C}}^{\text{prompt}}\right) \tag{5.9}$$

The data values and prompt yields of regions A, B and C as reported in Table 5.6 are used in Equation 5.9 to extract $N_{\text{D,exp}} = 31 \pm 19$. Uncertainties associated with the quantities measured in the ABCD method are computed using error propagation where it has been assumed that all the quantities are uncorrelated. The measured data values $N_{\text{A}}^{\text{Data}}$, $N_{\text{B}}^{\text{Data}}$ and $N_{\text{C}}^{\text{Data}}$ have Poissonian statistical uncertainties which have a dominant impact on the total uncertainty whereas uncertainties in the prompt yields estimated with MC simulation play a negligible role.

Region	**Data, N_i^{Data}**	**Prompt, N_i^{prompt}**	$N_i^{\text{Data}} - N_i^{\text{prompt}}$
A	28	0.68 ± 0.38	27.3 ± 5.3
B	9	3.92 ± 0.26	5.1 ± 3.0
C	166	0.98 ± 0.21	165 ± 13

Table 5.6: Data and yields in regions A, B and C used in Equation 5.9

The estimate for the non-prompt muon background in region D that was obtained from the closure test on MC is $N_D^{\text{MC}} = 23.1 \pm 5.9$ which differs by about 25% from the expected non-prompt muon background given by the data-driven ABCD method $N_{\text{D,exp}} = 31 \pm 19$. This is used later (Section 6.1) to introduce a systematic uncertainty on the MC non-prompt background.

5.4 A Note on Fake τ-Leptons

The τ-lepton has a mass of 1.776 GeV which allows it to decay not only into lighter leptons but also into hadrons approximately 65% of the time via the weak interaction. A τ-lepton can decay leptonically into a tau-neutrino, a lepton (electron or muon) and its corresponding neutrino. However, leptonically decaying τ-leptons are difficult to distinguish from prompt electrons and muons.

Hadronic decays of the τ-lepton usually result in a tau-neutrino, one or three charged pions (such that their total charge is ±1) and one (or more) neutral pion(s). Since charged particles leave tracks in the detectors, these decays are often classified as one- and three-pronged decays, where a prong denotes the charged track. Hadronically decaying τ-leptons (τ_{had}) can be identified as having low track multiplicities (one or three) and collimated clusters in calorimeters having a common secondary vertex (see Figure 5.8). However, there still remains a possibility of some misidentified candidates, originating mainly from electronic and hadronic jets due to the overlap of their signatures, to pass the selection criteria. Despite the fine granularity of the ECAL and various algorithms in place to differentiate between QCD jets and τ-jets [31], energy clusters originating from electrons can be mis-identified as those from neutral pion decays into photons and hadronic jets with low-track multiplicities can also be mis-identified as τ-jets. Such mis-identified candidates are called “fakes”.

For the purpose of this thesis, as the final state does not include electrons, fake τ-leptons from electronic jets can be neglected. However, the final state does consist of a light-quark and a b-quark, so fake τ-leptons can still originate from hadronic-jets. Due to a higher average track multiplicity of b-jets, they are less likely to be mis-identified as τ-leptons as compared to light-quark jets. Data-driven methods, like the Fake-Factor method, can be used to estimate the background from fake τ-leptons by defining control regions dominant in such a background and using an extrapolation factor (called the “fake factor”) to give the background in the signal region.

Such a method was used in certain search channels, namely, the 2ℓOS+1τ_{had} channel (which contains two leptons of opposite sign and one τ-lepton) in Reference [59], to estimate the background from fake τ-leptons. Given the similarity in the origin of τ_{had}-fakes in the different search channels, the obtained fake factor is then scaled to the 2ℓSS+1τ_{had} channel (which contains two leptons of

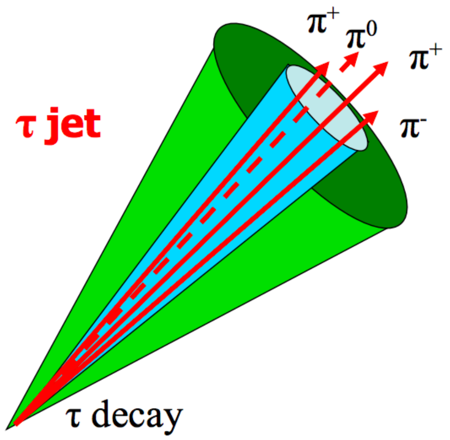

	tau	b quark
Mass	1.78 GeV	4.7 GeV
Lifetime	0.29 ps	1.5 ps
Decay length	87 μm	500 μm

Figure 5.8: A τ-lepton can decay hadronically into charged and neutral pions (and also a tau-neutrino, not shown here) which form a collimated stream of particles emnating from a secondary vertex, therefore also called a "τ-jet". Highly differing masses, lifetimes and decay lengths of a τ-lepton and a b-quark enable separation between a τ-jet and a b-jet. Illustration here depicts a three-prong decay and is taken from [58].

same sign and one τ-lepton). The 2ℓSS+$1\tau_{\text{had}}$ channel is quite similar in its signature to that of the cLFV signal of this thesis, the main exception being the jet-multiplicity. The 2ℓSS+$1\tau_{\text{had}}$ channel of the aforementioned Reference requires at least four jets whereas the signal in this thesis requires at least two, one of which is a b-jet. The "scale factor" for the 2ℓSS+$1\tau_{\text{had}}$ channel is computed in the 2ℓOS+$1\tau_{\text{had}}$ control region, which consists of at least three jets and no b-jets, as 1.36 ± 0.16. However, it is challenging to define an orthogonal control region enriched with τ_{had}-fakes for our signal by placing a cut on the jet multiplicity. Despite the constraints on time that limited further exploration in this direction, it should be noted that as fake backgrounds are not very well modelled by MC simulations, their estimation from data forms an important part of such analyses.

CHAPTER 6

Results

This chapter reports the systematic uncertainties considered in this analysis and the results of the fit to the data in order to test for the presence of a signal. The fit has been performed using the TRExFitter software framework [60] that implements the HistFactory toolkit [61].

6.1 Systematic Uncertainties

Systematic uncertainties are caused by instruments, techniques, assumptions and calibrations used to make a measurement and are not due to statistical chance. In this analysis, the following sources of systematic uncertainties have been considered:

Uncertainty on the data-driven estimation of non-prompt background The difference between the data-driven estimate of the non-prompt background and that from simulation is applied as a systematic uncertainty on events that contain at least one non-prompt muon, inclusively of taus.

The estimate for the non-prompt muon background in region D that was obtained from the closure test on MC is $N_D^{\text{MC}} = 23.1 \pm 5.9$ which differs by about 25% from the expected non-prompt muon background given by the data-driven ABCD method $N_{\text{D,exp}} = 31 \pm 19$. It is used to define a "scale factor" given by Equation 6.1.

$$\text{Scale Factor (SF)} = \frac{N_{\text{D,exp}}}{N_{\text{D,MC}}} \tag{6.1}$$

The value obtained for SF is 1.24 ± 0.79 which contains a large uncertainty (64%). Therefore, instead of "scaling" the background, the SF is used to introduce a systematic uncertainty on the MC non-prompt background estimation.

Instrumental uncertainties Detector effects can generate uncertainties on reconstruction, identification and trigger efficiencies as well as on momentum scales and resolutions for leptons. Uncertainties on the $E_{\text{T}}^{\text{miss}}$ scale, pileup effects, jet energy scale and resolution, flavour-tagging of jets and luminosity are also considered.

- Luminosity: The uncertainty on the integrated luminosity of the 2015 and 2016 datasets used in this analysis is 3.2% [62].

- Muon Reconstruction, Identification and Trigger: The reconstruction, identification and trigger efficiencies for muons vary between data and simulation. The nuisance parameters[1] related to the derived scale factors and their uncertainties are used as systematic uncertainties.
- Muon Momentum Scale and Resolution: These corrections are applied only on simulation and uncertainties on them are considered from both, the muon spectrometer and the ID.
- Pile-up and JVT: Uncertainties in pileup reweighing[2] and Jet Vertex Tagger efficiency are also included.
- Jet Energy Scale (JES) and Jet Energy Resolution (JER): The JES uncertainty accounts for the difference between the jet energy measurement of data and simulation, based on calibration studies. Performance of jet reconstruction is quantified by both, JES and JER, and their uncertainties are included in the systematics.
- Missing Transverse Momentum: Since the missing transverse momentum is reconstructed with the help of other reconstructed objects, uncertainties in the latter are also propagated to its measurement and are accounted for as systematic uncertainties.
- Heavy- and Light- Flavour Tagging: Efficiencies of heavy-flavour identification for jets are measured from data and are flavour-dependent. In simulation, these efficiencies are corrected by p_{T}-dependent factors while light-jet efficiencies also depend on η. Uncertainties in efficiencies of b-tagging, c-tagging and light flavour tagging are included.
- Tau Energy Scale (TES): Dedicated methods, similar to those for jets, are used [63] to measure TES shifts between simulation and data and their uncertainties, which are also included in the systematic uncertainties.

Theoretical uncertainties on cross-sections Cross-section uncertainties arising from theory are taken from Reference [2] and applied for background processes as listed in Table 6.1.

Process	Uncertainty (%)
Diboson	6
$t\bar{t}H$	+6.8, -9.9
$t\bar{t}W$	12.7
$t\bar{t}Z$	11.2
Others	50
VVV	5

Table 6.1: Theoretical uncertainties on cross-sections of background processes.

[1] The concept of nuisance parameters is introduced in Section 2.8.

[2] Pileup is generated when the detector measures objects that do not come from the primary vertex which is directly related to the average number of interactions that take place per bunch crossing. Since MC samples are produced before or while taking data, they are fed with only a best-guess of the pileup which are then reweighed to what is found in data.

6.2 Exclusion Limit

The strategy of this analysis is to evaluate the signal strength parameter μ using the profile likelihood fit. The inputs to the fit procedure are the number of expected and observed events (as a single-bin distribution of events) in the Signal Region (defined in Section 5.1). The systematic uncertainties, assumed to be uncorrelated, are inlcuded in the fit as nuisance parameters which have a combined effect on the uncertainties of background.

Prior to unblinding the data, the expected performance of the fit is studied using an Asimov dataset and reported in Appendix C. Here, an expected limit is set on the null hypothesis (signal plus background) at the 95% confidence level using the modified frequentist approach (CL_s method [64]). For each systematic uncertainty, the shape or normalization components that correspond to a negligible (<0.1%) background variation are dropped. The expected upper limit on the branching ratio $\mathrm{BR}(t \to \mu\tau q)$ is

$$\mathrm{BR}(t_{\mathrm{LFV}} \to \mu\tau q) < 1.00^{+1.45}_{-0.72} \times 10^{-4}.$$

Post unblinding, the data is found to be compatible with the absence of a signal. A background-only fit is performed on data and the observed limit on the branching ratio, computed in the same way as for the expected, is found to be

$$\mathrm{BR}(t_{\mathrm{LFV}} \to \mu\tau q) < 0.96 \times 10^{-4}.$$

The pre-fit and post-fit distributions in the Signal Region are shown in Figure 6.1 and the event yields are reported in Table 6.2. A total of eight events are recorded in the Signal Region. The fit improves the compatibility between data and background by reducing the $t\bar{t}$background which is the major contributor to the non-prompt muon background, and also constrains the uncertainty on the background. According to the ranking plot of the nuisance parameters (Figure 6.3(a)), the non-prompt scaling, which is the systematic uncertainty derived for the non-prompt muon background in Section 6.1, has the largest impact on the fit, followed by systematic uncertainties arising from the Jet Energy Resolution and Jet Energy Scale. The correlations between the systematic uncertainties are shown in Figure 6.2, where, as expected, the nuisance parameters are uncorrelated. Their pulls are shown in Figure 6.3(b) where the three paramters with the highest impact on the fit are slightly shifted (pulled) from their nominal zero value.

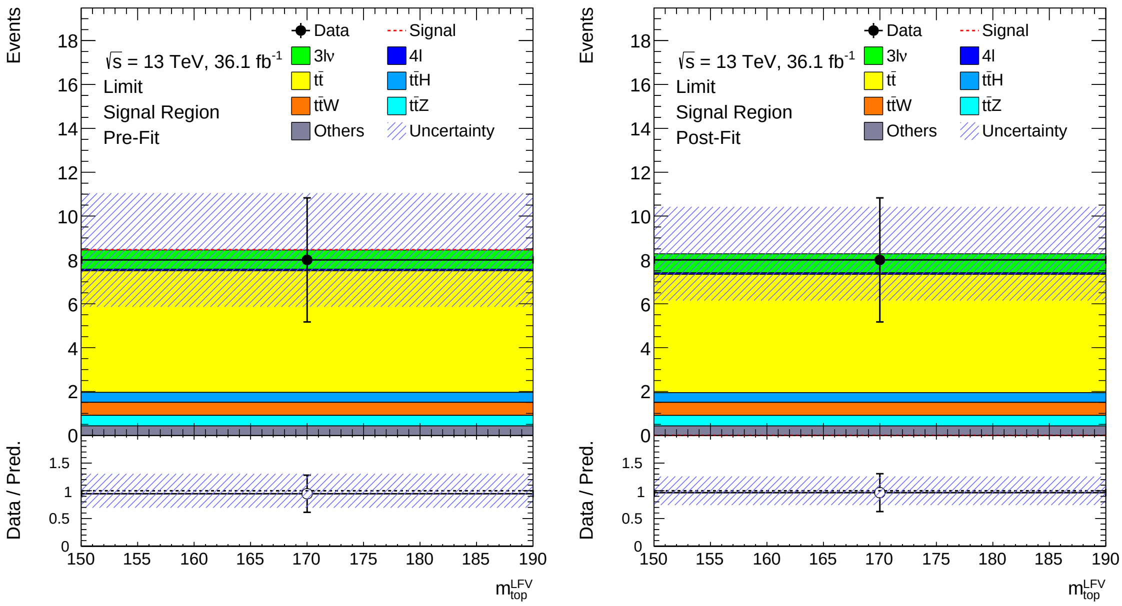

(a) (b)

Figure 6.1: (a) Pre-Fit and (b) Post-Fit distributions of the LFV top invariant mass in the Signal Region. The VVV, Z + jets and W + jets backgrounds are included in "Others".

Sample	**Pre-Fit**	**Post-Fit**
$3\ell\nu$	0.87 ± 0.39	0.87 ± 0.39
4ℓ	0.07 ± 0.03	0.07 ± 0.02
$t\bar{t}$	5.5 ± 2.4	5.4 ± 2.0
$t\bar{t}H$	0.45 ± 0.21	0.44 ± 0.19
$t\bar{t}W$	0.59 ± 0.11	0.59 ± 0.11
$t\bar{t}Z$	0.48 ± 0.09	0.48 ± 0.09
Others	0.43 ± 0.18	0.43 ± 0.18
Total Bkg.	8.5 ± 2.6	8.3 ± 2.1
Signal	8.5 ± 0.7	
S/B	(100 ± 32)%	
Data	8	8

Table 6.2: Pre-Fit and Post-Fit Yields in the Signal Region. The VVV, Z + jets and W + jets backgrounds are included in "Others".

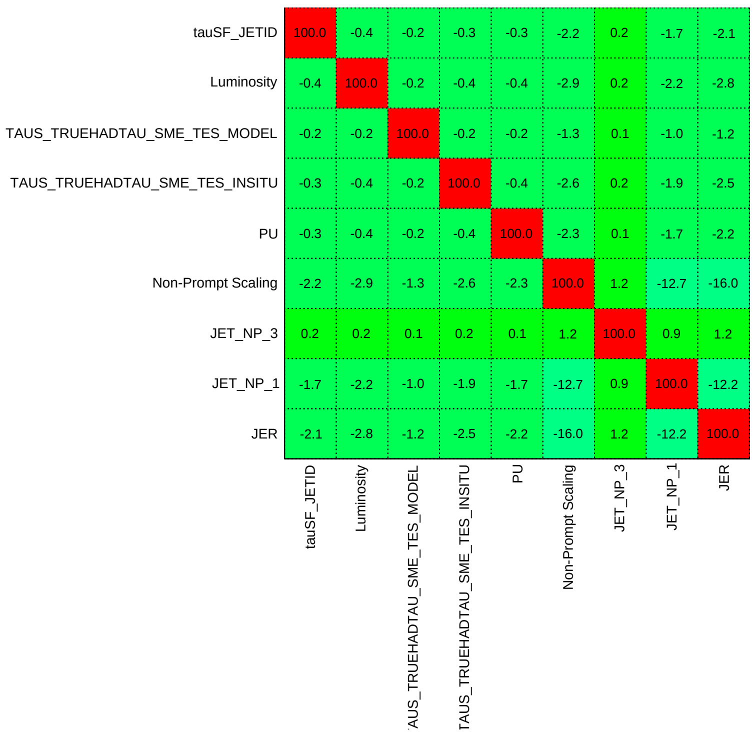

Figure 6.2: Correlations among nuisance parameters as measured by a background-only fit to data. Only NPs with at least one correlation entry larger than 1% are shown.

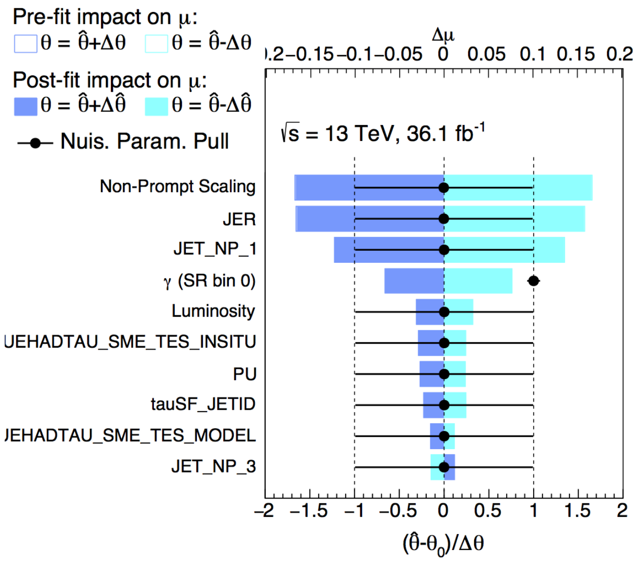

(a)

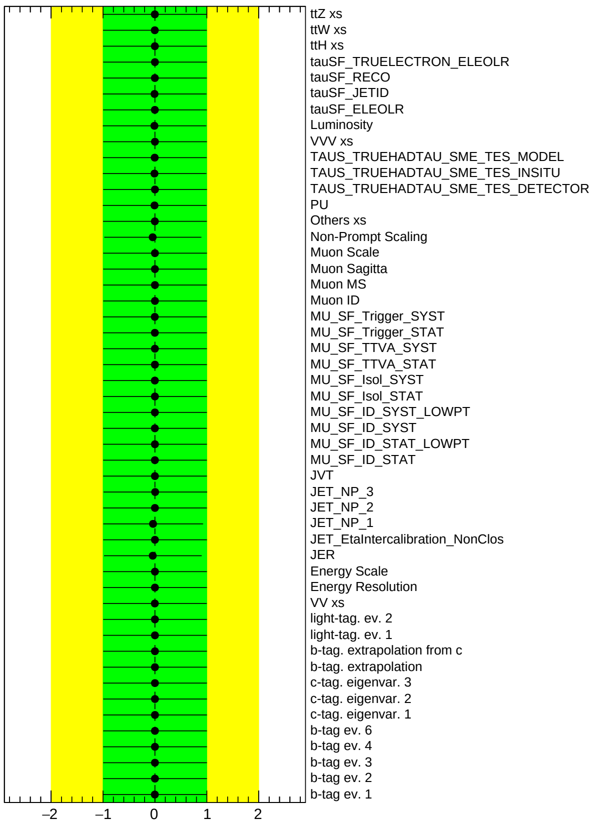

(b)

Figure 6.3: (a) Ranking and pulls of the nuisance parameters as measured by a background-only fit to data

CHAPTER 7

Conclusion

A first direct search for charged-lepton flavour violation in top-quark decays to the $\mu-\tau$ final state using data collected from proton-proton collisions at the LHC at a centre-of-mass energy of $\sqrt{s} = 13$ TeV, corresponding to an integrated luminosity of 36.1 fb^{-1}, as detected by the ATLAS experiment is presented in this analysis. The search was performed by studying top-quark pair events where one quark underwent a LFV decay $t(\bar{t}) \to \ell^{\pm}\ell'^{\mp}q(\overline{q})$, where $q \in u, c$ and $\ell \in \mu, \tau$ while the other top decayed according to the SM into a b-quark and a leptonically-decaying W-boson. The final-state topology, therefore, features two muons of the same electric charge, one τ-lepton, at least two jets and missing transverse momentum due to an undetected neutrino. No evidence for a signal was found and an observed (expected) upper limit on the branching ratio of $t_{\text{LFV}} \to \mu\tau q$ is presented as 0.96 (1.00) $\times 10^{-4}$ at the 95% confidence level.

Although the channel under study has a high signal-to-background ratio, it is limited in statistics. The use of machine-learning techniques, namely Boosted Decision Trees, was initially touched upon but later rejected given the low event yields. An overwhelming presence of non-prompt muons from $t\bar{t}$ events was handled using a data-driven technique called the ABCD method. However, it resulted in a "scale factor" with a very high uncertainty due to the statistically limited ABCD regions. The number of events in the four ABCD regions was also not parametrized on any kinematic variable due to the low statistics which made the ABCD technique itself prone to high statistical uncertainties (dominance of the Poissonian uncertainties on data). The scale factor is used to introduce a systematic uncertainty on the non-prompt muon background. Since the ABCD method is based entirely in the Pre-Selection Region and the systematic uncertainty is introduced in the Signal Region only, MC agreement with data in the Validation Region is not affected. For the sake of completeness, the systematic uncertainty in introduced in the Validation Region on non-prompt background events from MC simulation and the corresponding distributions of the kinematic variables are given in Appendix D.

The presence of fake τ-leptons, which could arise from mis-identification of jets, has not been accounted for in this thesis. However, a study was made of the $2\ell SS + 1\tau_{\text{had}}$ channel in [59] which is similar to the search channel of this thesis, except the higher jet multiplicity in the Reference. Unfortunately, further investigation in this direction was beyond the scope of the timescale of this analysis. As such, future prospects for investigating data-driven methods to estimate background from τ-fakes remain available.

Another important future prospect of this analysis lies in the interpretation of the upper limit on the branching ratio in terms of constraints on the EFT operators responsible for cLFV interactions.

Bibliography

[1] I. C. Brock,
Users Guide to Writing a Thesis in a Physics/Astronomy Institute of the Universität Bonn,
URL: http://pi.physik.uni-bonn.de/pi_only/thesis.php (cit. on p. iii).

[2] ATLAS Collaboration, *Search for charged lepton-flavour violation in top-quark decays at the LHC with the ATLAS detector*, (2018), URL: https://cds.cern.ch/record/2638305
(cit. on pp. 2, 22, 44).

[3] J. Ellis, *TikZ-Feynman: Feynman diagrams with TikZ*,
Comput. Phys. Commun. **210** (2017) 103, arXiv: 1601.05437 [hep-ph]
(cit. on pp. 2, 21, 36).

[4] G. Cowan et al., *Asymptotic formulae for likelihood-based tests of new physics*,
Eur. Phys. J. **C71** (2011) 1554, [Erratum: Eur. Phys. J.C73,2501(2013)],
arXiv: 1007.1727 [physics.data-an] (cit. on pp. 3, 9).

[5] C. Bini, *Data Analysis in Particle Phyiscs*, 2018, URL:
http://www.roma1.infn.it/people/bini/StatEPP_new.pdf (visited on 29/09/2018)
(cit. on p. 3).

[6] S. L. Glashow, *Partial Symmetries of Weak Interactions*, Nucl. Phys. **22** (1961) 579
(cit. on p. 3).

[7] S. Weinberg, *A Model of Leptons*, Phys. Rev. Lett. **19** (1967) 1264 (cit. on p. 3).

[8] A. Salam, *Weak and Electromagnetic Interactions*, Conf. Proc. **C680519** (1968) 367
(cit. on p. 3).

[9] M. Thomson, *Modern particle physics*, Cambridge University Press, 2013,
ISBN: 9781107034266, URL:
http://www-spires.fnal.gov/spires/find/books/www?cl=QC793.2.T46::2013
(cit. on pp. 3, 5, 6, 11).

[10] L. Calibbi and G. Signorelli,
Charged Lepton Flavour Violation: An Experimental and Theoretical Introduction,
Riv. Nuovo Cim. **41** (2018) 1, arXiv: 1709.00294 [hep-ph] (cit. on pp. 5, 7).

[11] Q. R. Ahmad et al., *Direct evidence for neutrino flavor transformation from neutral current interactions in the Sudbury Neutrino Observatory*, Phys. Rev. Lett. **89** (2002) 011301,
arXiv: nucl-ex/0204008 (cit. on p. 6).

[12] Y. Fukuda et al., *Evidence for oscillation of atmospheric neutrinos*,
Phys. Rev. Lett. **81** (1998) 1562, arXiv: hep-ex/9807003 (cit. on p. 6).

[13] L. Maiani, “The GIM Mechanism: origin, predictions and recent uses”, *Proceedings, 48th Rencontres de Moriond on Electroweak Interactions and Unified Theories: La Thuile, Italy, March 2-9, 2013*, 2013 3, arXiv: 1303.6154 [hep-ph] (cit. on p. 7).

[14] A. M. Teixeira, *Theoretical aspects of charged Lepton Flavour Violation*, J. Phys. Conf. Ser. **888** (2017) 012029, arXiv: 1612.05561 [hep-ph] (cit. on p. 7).

[15] A. Abada, “Neutrino Physics, Lepton Flavour Violation and the LHC”, *25th Rencontres de Blois on Particle Physics and Cosmology Blois, France, May 26-31, 2013*, 2013, arXiv: 1310.3800 [hep-ph] (cit. on p. 7).

[16] A. A. Petrov and A. E. Blechman, *Effective Field Theories*, WSP, 2016, URL: http://www.worldscientific.com/worldscibooks/10.1142/8619 (cit. on p. 7).

[17] M. Carpentier and S. Davidson, *Constraints on two-lepton, two quark operators*, Eur. Phys. J. **C70** (2010) 1071, arXiv: 1008.0280 [hep-ph] (cit. on p. 7).

[18] S. Davidson et al., *Lepton Flavour Violating top decays at the LHC*, Eur. Phys. J. **C75** (2015) 450, arXiv: 1507.07163 [hep-ph] (cit. on pp. 7, 21, 22).

[19] M. Kobayashi and T. Maskawa, *CP Violation in the Renormalizable Theory of Weak Interaction*, Prog. Theor. Phys. **49** (1973) 652 (cit. on p. 8).

[20] F. Abe et al., *Observation of top quark production in $\bar{p}p$ collisions*, Phys. Rev. Lett. **74** (1995) 2626, arXiv: hep-ex/9503002 (cit. on p. 8).

[21] S. Abachi et al., *Observation of the top quark*, Phys. Rev. Lett. **74** (1995) 2632, arXiv: hep-ex/9503003 [hep-ex] (cit. on p. 8).

[22] M. Tanabashi et al., *Review of Particle Physics*, Phys. Rev. D **98** (2018) 030001 (cit. on pp. 8, 22).

[23] N. Bruscino, *A gateway to new physics: direct measurement of the top Yukawa coupling to the Higgs boson*, PhD Thesis, 2017, URL: https://cds.cern.ch/record/2273695 (cit. on p. 8).

[24] M. Cristinziani and M. Mulders, *Top-quark physics at the Large Hadron Collider*, J. Phys. **G44** (2017) 063001, arXiv: 1606.00327 [hep-ex] (cit. on p. 8).

[25] *Diagram showing the common principle of identification of jets initiated by b-hadron decays*, 2016, URL: http://bartosik.pp.ua/hep_sketches/btagging (visited on 05/10/2018) (cit. on p. 14).

[26] P. La Rocca and F. Riggi, *The upgrade programme of the major experiments at the Large Hadron Collider*, J. Phys. Conf. Ser. **515** (2014) 012012 (cit. on p. 14).

[27] ATLAS Collaboration, *Observation of a new particle in the search for the Standard Model Higgs boson with the ATLAS detector at the LHC*, Phys. Lett. **B716** (2012) 1, arXiv: 1207.7214 [hep-ex] (cit. on p. 14).

[28] S. Chatrchyan et al., *Observation of a new boson at a mass of 125 GeV with the CMS experiment at the LHC*, Phys. Lett. **B716** (2012) 30, arXiv: 1207.7235 [hep-ex] (cit. on p. 14).

[29] E. Mobs, *The CERN accelerator complex. Complexe des accélérateurs du CERN*, (2016), General Photo, URL: https://cds.cern.ch/record/2197559 (cit. on p. 15).

[30] M. A. et al. (ATLAS Collaboration), *ATLAS Luminosity Public Results (Run 2)*, 2018, URL: https://twiki.cern.ch/twiki/bin/view/AtlasPublic/LuminosityPublicResultsRun2 (visited on 20/09/2018) (cit. on p. 15).

[31] ATLAS Collaboration, *The ATLAS Experiment at the CERN Large Hadron Collider*, JINST **3** (2008) S08003 (cit. on pp. 14, 16, 18–20, 41).

[32] M. Capeans et al., *ATLAS Insertable B-Layer Technical Design Report*, (2010), URL: https://cds.cern.ch/record/1291633 (cit. on p. 17).

[33] ATLAS Collaboration, *Expected performance of the ATLAS b-tagging algorithms in Run-2*, (2015), URL: https://cds.cern.ch/record/2037697 (cit. on p. 17).

[34] J. G. Panduro Vazquez, *The ATLAS Data Acquisition System: from Run 1 to Run 2*, (2014), URL: https://cds.cern.ch/record/1954156 (cit. on pp. 19, 20).

[35] J. Stelzer, *The ATLAS High Level Trigger Configuration and Steering, Experience with the First 7 TeV Collisions*, (2011), URL: https://cds.cern.ch/record/1337002 (cit. on p. 20).

[36] *ATLAS Trigger and Data Acquisition System*, 2018, URL: https//atlas.cern/discover/detector/trigger-daq (visited on 19/09/2018) (cit. on p. 20).

[37] T. Sjöstrand et al., *An Introduction to PYTHIA 8.2*, Comput. Phys. Commun. **191** (2015) 159, arXiv: 1410.3012 [hep-ph] (cit. on p. 22).

[38] S. Agostinelli et al., *GEANT4: A Simulation toolkit*, Nucl. Instrum. Meth. **A506** (2003) 250 (cit. on p. 22).

[39] M. Czakon, P. Fiedler and A. Mitov, *Total Top-Quark Pair-Production Cross Section at Hadron Colliders Through $O(\alpha_S^4)$*, Phys. Rev. Lett. **110** (2013) 252004, arXiv: 1303.6254 [hep-ph] (cit. on p. 22).

[40] L. T. W. Group, *NNLO+NNLL top-quark-pair cross sections*, 2015, URL: https://twiki.cern.ch/twiki/bin/view/LHCPhysics/TtbarNNLO (visited on 20/09/2018) (cit. on p. 22).

[41] ATLAS Collaboration, *Muon reconstruction performance of the ATLAS detector in proton–proton collision data at $\sqrt{s}$ =13 TeV*, Eur. Phys. J. **C76** (2016) 292, arXiv: 1603.05598 [hep-ex] (cit. on p. 23).

[42] ATLAS Collaboration, *Electron efficiency measurements with the ATLAS detector using 2012 LHC proton–proton collision data*, Eur. Phys. J. **C77** (2017) 195, arXiv: 1612.01456 [hep-ex] (cit. on p. 24).

[43] A. Hrynevich, *ATLAS jet and missing energy reconstruction, calibration and performance in LHC Run-2*, JINST **12** (2017) C06038 (cit. on p. 25).

[44] ATLAS Collaboration,
Topological cell clustering in the ATLAS calorimeters and its performance in LHC Run 1, Eur. Phys. J. **C77** (2017) 490, arXiv: 1603.02934 [hep-ex] (cit. on p. 25).

[45] M. Cacciari, G. P. Salam and G. Soyez, *The anti-k_t jet clustering algorithm*, JHEP **04** (2008) 063, arXiv: 0802.1189 [hep-ph] (cit. on p. 25).

[46] ATLAS Collaboration, *Tagging and suppression of pileup jets with the ATLAS detector*, (2014), URL: https://cds.cern.ch/record/1700870 (cit. on pp. 25, 26).

[47] ATLAS Collaboration,
Optimisation of the ATLAS b-tagging performance for the 2016 LHC Run, (2016), URL: https://cds.cern.ch/record/2160731 (cit. on p. 25).

[48] ATLAS Collaboration, *Reconstruction, Energy Calibration, and Identification of Hadronically Decaying Tau Leptons in the ATLAS Experiment for Run-2 of the LHC*, (2015), URL: https://cds.cern.ch/record/2064383 (cit. on p. 25).

[49] ATLAS Collaboration, *Performance of algorithms that reconstruct missing transverse momentum in $\sqrt{s}$ = 8 TeV proton-proton collisions in the ATLAS detector*, Eur. Phys. J. **C77** (2017) 241, arXiv: 1609.09324 [hep-ex] (cit. on p. 25).

[50] D. Adams et al.,
Recommendations of the Physics Objects and Analysis Harmonisation Study Groups 2014, (2014), URL: https://cds.cern.ch/record/1743654 (cit. on p. 25).

[51] S. Farrell, *Overlap Removal Tools*, 2016,
URL: https://indico.cern.ch/event/539619/contributions/2191033/attachments/1284239/1909241/Farrell_ort_asg.pdf (visited on 20/09/2018) (cit. on p. 25).

[52] M. Cacciari, G. P. Salam and G. Soyez, *The Catchment Area of Jets*, JHEP **04** (2008) 005, arXiv: 0802.1188 [hep-ph] (cit. on p. 26).

[53] K. Grimm, *Primary Vertex Reconstruction at the ATLAS Experiment*, 2016,
URL: https://indico.cern.ch/event/505613/contributions/2230823/attachments/1347540/2046950/130-Oral.pdf (visited on 20/09/2018) (cit. on p. 26).

[54] F. Meloni, *ATLAS Vertexing Group: Run 2 Recommendations*, 2018,
URL: https://twiki.cern.ch/twiki/bin/view/Main/VertexingGroup (visited on 20/09/2018) (cit. on p. 26).

[55] T. Chwalek,
Messung der W-Boson-Helizitätsanteile in Top-Quark-Zerfällen mit dem CDF II Experiment und Studien zu einer frühen Messung des ttbar-Wirkungsquerschnitts mit dem CMS Experiment, PhD Thesis, 2010, URL: https://cds.cern.ch/record/1416031 (cit. on p. 31).

[56] R. Brun and F. Rademakers, *ROOT: An object oriented data analysis framework*, Nucl. Instrum. Meth. **A389** (1997) 81 (cit. on p. 32).

[57] A. Loginov, *Strategies of data-driven estimations of ttbar backgrounds in ATLAS*, (2010), URL: https://cds.cern.ch/record/1287126 (cit. on p. 36).

[58] Y. Coadou, *Tau trigger and tau reconstruction, efficiency and fake rates in ATLAS*, (2010), URL: https://cds.cern.ch/record/1304290 (cit. on p. 42).

[59] ATLAS Collaboration, *Evidence for the associated production of the Higgs boson and a top quark pair with the ATLAS detector*, Phys. Rev. **D97** (2018) 072003, arXiv: 1712.08891 [hep-ex] (cit. on pp. 41, 49).

[60] *TRExFitter Framework - ATLAS Protected Page*, 2018, URL: https://twiki.cern.ch/twiki/bin/viewauth/AtlasProtected/TtHFitter (visited on 2018) (cit. on p. 43).

[61] K. Cranmer et al., *HistFactory: A tool for creating statistical models for use with RooFit and RooStats*, (2012), URL: https://cds.cern.ch/record/1456844 (cit. on p. 43).

[62] R. Hawkings, *Luminosity For Physics*, 2018, URL: https://twiki.cern.ch/twiki/bin/viewauth/Atlas/LuminosityForPhysics#2015_13_TeV_proton_proton_final (visited on 20/09/2018) (cit. on p. 43).

[63] ATLAS Collaboration, *Identification and energy calibration of hadronically decaying tau leptons with the ATLAS experiment in pp collisions at* $\sqrt{s}$*=8 TeV*, Eur. Phys. J. **C75** (2015) 303, arXiv: 1412.7086 [hep-ex] (cit. on p. 44).

[64] A. L. Read, *Presentation of search results: The CL(s) technique*, J. Phys. **G28** (2002) 2693, [,11(2002)] (cit. on p. 45).

APPENDIX A

List of MC Simulation Samples

Process	Dataset ID	Name
Signal		
	410775	MadGraphPythia8EvtGen_A14NNPDF23_ttbarLFV_lept_DF
4ℓ		
	345705	Sherpa_222_NNPDF30NNLO_gglll l_0M4l130
	345706	Sherpa_222_NNPDF30NNLO_ggllll_130M4l
	364250	Sherpa_222_NNPDF30NNLO_llll
	364283	Sherpa_222_NNPDF30NNLO_lllljj_EW6
	364288	Sherpa_222_NNPDF30NNLO_llll_lowMllPtComplement
$3\ell\nu$		
	364253	Sherpa_222_NNPDF30NNLO_lllv
	364284	Sherpa_222_NNPDF30NNLO_lllvjj_EW6
	364289	Sherpa_222_NNPDF30NNLO_lllv_lowMllPtComplement
$\ell\nu qq$		
$t\bar{t}$		
	410470	PhPy8EG_A14_ttbar_hdamp258p75_nonallhad
$t\bar{t}\gamma$		
	410389	MadGraphPythia8EvtGen_A14NNPDF23_ttgamma_nonallhadronic
$t\bar{t}H$		
	345673	PowhegPythia8EvtGen_A14NNPDF23_NNPDF30ME_ttH125_semilep
	345674	PowhegPythia8EvtGen_A14NNPDF23_NNPDF30ME_ttH125_dilep
$t\bar{t}W$		
	410155	aMcAtNloPythia8EvtGen_MEN30NLO_A14N23LO_ttW
$t\bar{t}Z$		
	410218	aMcAtNloPythia8EvtGen_MEN30NLO_A14N23LO_ttee
	410219	aMcAtNloPythia8EvtGen_MEN30NLO_A14N23LO_ttmumu
	410220	aMcAtNloPythia8EvtGen_MEN30NLO_A14N23LO_tttautau

Table A.1: Samples used for the MC simulation from the MC16a production campaign (Part 1/4)

Process	Dataset ID	Name
$Z + \gamma$		
	364500	Sherpa_222_NNPDF30NNLO_eegamma_pty_7_15
	364501	Sherpa_222_NNPDF30NNLO_eegamma_pty_15_35
	364502	Sherpa_222_NNPDF30NNLO_eegamma_pty_35_70
	364503	Sherpa_222_NNPDF30NNLO_eegamma_pty_70_140
	364504	Sherpa_222_NNPDF30NNLO_eegamma_pty_140_E_CMS
	364505	Sherpa_222_NNPDF30NNLO_mumugamma_pty_7_15
	364506	Sherpa_222_NNPDF30NNLO_mumugamma_pty_15_35
	364507	Sherpa_222_NNPDF30NNLO_mumugamma_pty_35_70
	364508	Sherpa_222_NNPDF30NNLO_mumugamma_pty_70_140
	364509	Sherpa_222_NNPDF30NNLO_mumugamma_pty_140_E_CMS
	364510	Sherpa_222_NNPDF30NNLO_tautaugamma_pty_7_15
	364511	Sherpa_222_NNPDF30NNLO_tautaugamma_pty_15_35
	364512	Sherpa_222_NNPDF30NNLO_tautaugamma_pty_35_70
	364513	Sherpa_222_NNPDF30NNLO_tautaugamma_pty_70_140
	364514	Sherpa_222_NNPDF30NNLO_tautaugamma_pty_140_E_CMS
VVV		
	364242	Sherpa_222_NNPDF30NNLO_WWW_3l3v_EW6
	364243	Sherpa_222_NNPDF30NNLO_WWZ_4l2v_EW6
	364244	Sherpa_222_NNPDF30NNLO_WWZ_2l4v_EW6
	364245	Sherpa_222_NNPDF30NNLO_WZZ_5l1v_EW6
	364246	Sherpa_222_NNPDF30NNLO_WZZ_3l3v_EW6
	364247	Sherpa_222_NNPDF30NNLO_ZZZ_6l0v_EW6
	364248	Sherpa_222_NNPDF30NNLO_ZZZ_4l2v_EW6
	364249	Sherpa_222_NNPDF30NNLO_ZZZ_2l4v_EW6
$t + X$		
	410011	PowhegPythiaEvtGen_P2012_singletop_tchan_lept_top
	410012	PowhegPythiaEvtGen_P2012_singletop_tchan_lept_antitop
	410013	PowhegPythiaEvtGen_P2012_Wt_inclusive_top
	410014	PowhegPythiaEvtGen_P2012_Wt_inclusive_antitop
	410560	MadGraphPythia8EvtGen_A14_tZ_4fl_tchan_noAllHad
	410408	aMcAtNloPythia8EvtGen_tWZ_Ztoll_minDR1
	410025	PowhegPythiaEvtGen_P2012_SingleTopSchan_noAllHad_top
	410026	PowhegPythiaEvtGen_P2012_SingleTopSchan_noAllHad_antitop
Others:		
	363356	Sherpa_221_NNPDF30NNLO_ZqqZll
	363358	Sherpa_221_NNPDF30NNLO_WqqZll
	364254	Sherpa_222_NNPDF30NNLO_llvv
	364285	Sherpa_222_NNPDF30NNLO_llvvjj_EW6
	364287	Sherpa_222_NNPDF30NNLO_llvvjj_ss_EW6
	304014	MadGraphPythia8EvtGen_A14NNPDF23_3top_SM
	342284	Pythia8EvtGen_A14NNPDF23LO_WH125_inc
	342285	Pythia8EvtGen_A14NNPDF23LO_ZH125_inc
	345060	PowhegPythia8EvtGen_NNLOPS_nnlo_30_ggH125_ZZ4l
	410080	MadGraphPythia8EvtGen_A14NNPDF23_4topSM
	410081	MadGraphPythia8EvtGen_A14NNPDF23_ttbarWW

Table A.2: Samples used for the MC simulation from the MC16a production campaign (Part 2/4)

Process	Dataset ID	Name
***W* + jets**		
	364156	Sherpa_221_NNPDF30NNLO_Wmunu_MAXHTPTV0_70_CVetoBVeto
	364157	Sherpa_221_NNPDF30NNLO_Wmunu_MAXHTPTV0_70_CFilterBVeto
	364158	Sherpa_221_NNPDF30NNLO_Wmunu_MAXHTPTV0_70_BFilter
	364159	Sherpa_221_NNPDF30NNLO_Wmunu_MAXHTPTV70_140_CVetoBVeto
	364160	Sherpa_221_NNPDF30NNLO_Wmunu_MAXHTPTV70_140_CFilterBVeto
	364161	Sherpa_221_NNPDF30NNLO_Wmunu_MAXHTPTV70_140_BFilter
	364162	Sherpa_221_NNPDF30NNLO_Wmunu_MAXHTPTV140_280_CVetoBVeto
	364163	Sherpa_221_NNPDF30NNLO_Wmunu_MAXHTPTV140_280_CFilterBVeto
	364164	Sherpa_221_NNPDF30NNLO_Wmunu_MAXHTPTV140_280_BFilter
	364165	Sherpa_221_NNPDF30NNLO_Wmunu_MAXHTPTV280_500_CVetoBVeto
	364166	Sherpa_221_NNPDF30NNLO_Wmunu_MAXHTPTV280_500_CFilterBVeto
	364167	Sherpa_221_NNPDF30NNLO_Wmunu_MAXHTPTV280_500_BFilter
	364168	Sherpa_221_NNPDF30NNLO_Wmunu_MAXHTPTV500_1000
	364169	Sherpa_221_NNPDF30NNLO_Wmunu_MAXHTPTV1000_E_CMS
	364170	Sherpa_221_NNPDF30NNLO_Wenu_MAXHTPTV0_70_CVetoBVeto
	364171	Sherpa_221_NNPDF30NNLO_Wenu_MAXHTPTV0_70_CFilterBVeto
	364172	Sherpa_221_NNPDF30NNLO_Wenu_MAXHTPTV0_70_BFilter
	364173	Sherpa_221_NNPDF30NNLO_Wenu_MAXHTPTV70_140_CVetoBVeto
	364174	Sherpa_221_NNPDF30NNLO_Wenu_MAXHTPTV70_140_CFilterBVeto
	364175	Sherpa_221_NNPDF30NNLO_Wenu_MAXHTPTV70_140_BFilter
	364176	Sherpa_221_NNPDF30NNLO_Wenu_MAXHTPTV140_280_CVetoBVeto
	364177	Sherpa_221_NNPDF30NNLO_Wenu_MAXHTPTV140_280_CFilterBVeto
	364178	Sherpa_221_NNPDF30NNLO_Wenu_MAXHTPTV140_280_BFilter
	364179	Sherpa_221_NNPDF30NNLO_Wenu_MAXHTPTV280_500_CVetoBVeto
	364180	Sherpa_221_NNPDF30NNLO_Wenu_MAXHTPTV280_500_CFilterBVeto
	364181	Sherpa_221_NNPDF30NNLO_Wenu_MAXHTPTV280_500_BFilter
	364182	Sherpa_221_NNPDF30NNLO_Wenu_MAXHTPTV500_1000
	364183	Sherpa_221_NNPDF30NNLO_Wenu_MAXHTPTV1000_E_CMS
	364184	Sherpa_221_NNPDF30NNLO_Wtaunu_MAXHTPTV0_70_CVetoBVeto
	364185	Sherpa_221_NNPDF30NNLO_Wtaunu_MAXHTPTV0_70_CFilterBVeto
	364186	Sherpa_221_NNPDF30NNLO_Wtaunu_MAXHTPTV0_70_BFilter
	364187	Sherpa_221_NNPDF30NNLO_Wtaunu_MAXHTPTV70_140_CVetoBVeto
	364188	Sherpa_221_NNPDF30NNLO_Wtaunu_MAXHTPTV70_140_CFilterBVeto
	364189	Sherpa_221_NNPDF30NNLO_Wtaunu_MAXHTPTV70_140_BFilter
	364190	Sherpa_221_NNPDF30NNLO_Wtaunu_MAXHTPTV140_280_CVetoBVeto
	364191	Sherpa_221_NNPDF30NNLO_Wtaunu_MAXHTPTV140_280_CFilterBVeto
	364192	Sherpa_221_NNPDF30NNLO_Wtaunu_MAXHTPTV140_280_BFilter
	364193	Sherpa_221_NNPDF30NNLO_Wtaunu_MAXHTPTV280_500_CVetoBVeto
	364194	Sherpa_221_NNPDF30NNLO_Wtaunu_MAXHTPTV280_500_CFilterBVeto
	364195	Sherpa_221_NNPDF30NNLO_Wtaunu_MAXHTPTV280_500_BFilter
	364196	Sherpa_221_NNPDF30NNLO_Wtaunu_MAXHTPTV500_1000
	364197	Sherpa_221_NNPDF30NNLO_Wtaunu_MAXHTPTV1000_E_CMS

Table A.3: Samples used for the MC simulation from the MC16a production campaign (Part 3/4)

Process	Dataset ID	Name
***Z* + jets**		
	364100	Sherpa_221_NNPDF30NNLO_Zmumu_MAXHTPTV0_70_CVetoBVeto
	364101	Sherpa_221_NNPDF30NNLO_Zmumu_MAXHTPTV0_70_CFilterBVeto
	364102	Sherpa_221_NNPDF30NNLO_Zmumu_MAXHTPTV0_70_BFilter
	364103	Sherpa_221_NNPDF30NNLO_Zmumu_MAXHTPTV70_140_CVetoBVeto
	364104	Sherpa_221_NNPDF30NNLO_Zmumu_MAXHTPTV70_140_CFilterBVeto
	364105	Sherpa_221_NNPDF30NNLO_Zmumu_MAXHTPTV70_140_BFilter
	364106	Sherpa_221_NNPDF30NNLO_Zmumu_MAXHTPTV140_280_CVetoBVeto
	364107	Sherpa_221_NNPDF30NNLO_Zmumu_MAXHTPTV140_280_CFilterBVeto
	364108	Sherpa_221_NNPDF30NNLO_Zmumu_MAXHTPTV140_280_BFilter
	364109	Sherpa_221_NNPDF30NNLO_Zmumu_MAXHTPTV280_500_CVetoBVeto
	364110	Sherpa_221_NNPDF30NNLO_Zmumu_MAXHTPTV280_500_CFilterBVeto
	364111	Sherpa_221_NNPDF30NNLO_Zmumu_MAXHTPTV280_500_BFilter
	364112	Sherpa_221_NNPDF30NNLO_Zmumu_MAXHTPTV500_1000
	364113	Sherpa_221_NNPDF30NNLO_Zmumu_MAXHTPTV1000_E_CMS
	364114	Sherpa_221_NNPDF30NNLO_Zee_MAXHTPTV0_70_CVetoBVeto
	364115	Sherpa_221_NNPDF30NNLO_Zee_MAXHTPTV0_70_CFilterBVeto
	364116	Sherpa_221_NNPDF30NNLO_Zee_MAXHTPTV0_70_BFilter
	364117	Sherpa_221_NNPDF30NNLO_Zee_MAXHTPTV70_140_CVetoBVeto
	364118	Sherpa_221_NNPDF30NNLO_Zee_MAXHTPTV70_140_CFilterBVeto
	364119	Sherpa_221_NNPDF30NNLO_Zee_MAXHTPTV70_140_BFilter
	364120	Sherpa_221_NNPDF30NNLO_Zee_MAXHTPTV140_280_CVetoBVeto
	364121	Sherpa_221_NNPDF30NNLO_Zee_MAXHTPTV140_280_CFilterBVeto
	364122	Sherpa_221_NNPDF30NNLO_Zee_MAXHTPTV140_280_BFilter
	364123	Sherpa_221_NNPDF30NNLO_Zee_MAXHTPTV280_500_CVetoBVeto
	364124	Sherpa_221_NNPDF30NNLO_Zee_MAXHTPTV280_500_CFilterBVeto
	364125	Sherpa_221_NNPDF30NNLO_Zee_MAXHTPTV280_500_BFilter
	364126	Sherpa_221_NNPDF30NNLO_Zee_MAXHTPTV500_1000
	364127	Sherpa_221_NNPDF30NNLO_Zee_MAXHTPTV1000_E_CMS
	364128	Sherpa_221_NNPDF30NNLO_Ztautau_MAXHTPTV0_70_CVetoBVeto
	364129	Sherpa_221_NNPDF30NNLO_Ztautau_MAXHTPTV0_70_CFilterBVeto
	364130	Sherpa_221_NNPDF30NNLO_Ztautau_MAXHTPTV0_70_BFilter
	364131	Sherpa_221_NNPDF30NNLO_Ztautau_MAXHTPTV70_140_CVetoBVeto
	364132	Sherpa_221_NNPDF30NNLO_Ztautau_MAXHTPTV70_140_CFilterBVeto
	364133	Sherpa_221_NNPDF30NNLO_Ztautau_MAXHTPTV70_140_BFilter
	364134	Sherpa_221_NNPDF30NNLO_Ztautau_MAXHTPTV140_280_CVetoBVeto
	364135	Sherpa_221_NNPDF30NNLO_Ztautau_MAXHTPTV140_280_CFilterBVeto
	364136	Sherpa_221_NNPDF30NNLO_Ztautau_MAXHTPTV140_280_BFilter
	364137	Sherpa_221_NNPDF30NNLO_Ztautau_MAXHTPTV280_500_CVetoBVeto
	364138	Sherpa_221_NNPDF30NNLO_Ztautau_MAXHTPTV280_500_CFilterBVeto
	364139	Sherpa_221_NNPDF30NNLO_Ztautau_MAXHTPTV280_500_BFilter
	364140	Sherpa_221_NNPDF30NNLO_Ztautau_MAXHTPTV500_1000
	364141	Sherpa_221_NNPDF30NNLO_Ztautau_MAXHTPTV1000_E_CMS

Table A.4: Samples used for the MC simulation from the MC16a production campaign (Part 4/4)

APPENDIX B

Calculation of the z-component of Neutrino Momentum

The decay of the W-boson into a lepton and a neutrino can be expressed in terms of Equation B.1 which originates from 4-momentum conservation between initial and final state particles.

$$p_W = p_\ell + p_\nu \tag{B.1}$$

Squaring this equation, we get

$$\begin{aligned} p_W^2 &= (p_\ell + p_\nu)^2 \\ &= p_\ell^2 + p_\nu^2 + 2p_\ell p_\nu \end{aligned} \tag{B.2}$$

Since the invariant mass m is related to the 4-momentum as $m^2 = p^2$, the above equation can be re-written as

$$m_W^2 = m_\ell^2 + m_\nu^2 + 2p_\ell p_\nu \tag{B.3}$$

Assuming that the invariant masses of the lepton and the neutrino are negligible compared to their energies,

$$\begin{aligned} m_W^2 &= 2p_\ell p_\nu \\ &= 2(E_\ell E_\nu - \boldsymbol{p_\ell p_\nu}) \\ &= 2(E_\ell E_\nu - p_{\mathrm{T},\ell} p_{\mathrm{T},\nu} \cos(\phi_\ell - \phi_\nu) - p_{z,\ell} p_{z,\nu} \end{aligned} \tag{B.4}$$

which can be rearranged to give

$$E_\ell E_\nu = \mu + p_{z,\ell} p_{z,\nu} \tag{B.5}$$

where $\mu = \frac{m_W^2}{2} + p_{\mathrm{T},\ell} p_{\mathrm{T},\nu} \cos(\Delta\phi)$ has been introduced. The energy of the massless neutrino E_ν can be written in terms of its momentum components in Equation B.5 which gives

$$E_\ell\sqrt{p_{\mathrm{T},\nu}^2 + p_{z,\nu}^2} = \mu + p_{z,\ell}p_{z,\nu} \tag{B.6}$$

On squaring the above equation and rearranging its terms, a quadratic equation given by B.7 is obtained.

$$p_{z,\nu}^2 - \left(\frac{2\mu p_{z,\ell}}{E_\ell^2 - p_{z,\ell}^2}\right)p_{z,\nu} + \frac{E_\ell^2 p_{\mathrm{T},\nu}^2 - \mu^2}{E_\ell^2 - p_{z,\ell}^2} = 0 \tag{B.7}$$

The z-component of the neutrino momentum are given by the solutions of this quadratic equation as

$$p_{z,\nu}^{\pm} = \frac{\mu p_{z,\ell}}{p_{\mathrm{T},\ell}^2} \pm \sqrt{\frac{\mu^2 p_{z,\ell}^2}{p_{\mathrm{T},\ell}^4} - \frac{E_\ell^2 p_{\mathrm{T},\nu}^2 - \mu^2}{p_{\mathrm{T},\ell}^2}} \tag{B.8}$$

APPENDIX C

Asimov Fits

An Asimov dataset is used to study the expected performance of the fit. The pre-fit yields are reported in Table C.1. A signal plus background fit corresponding to signal strength $\mu = 0$ is performed on an Asimov dataset. Figure C.2(a) shows the ranking of the nuisance parameters according to their impact on the fitted μ. The highest impact on the fit is from the uncertainty introduced by non-prompt scaling, which is the systematic uncertainty derived for the non-prompt muon background in Section 6.1, followed by systematic uncertainties arising from the Jet Energy Resolution and Jet Energy Scale. The correlations between the nuisance parameters (which are assumed to be uncorrelated) are shown in Figure C.1 and their pulls are shown in Figure C.2(b).

Sample	**Pre-Fit**
$3\ell\nu$	0.87 ± 0.39
4ℓ	0.07 ± 0.03
Others	0.10 ± 0.07
$t\bar{t}$	5.4 ± 2.4
$t\bar{t}H$	0.45 ± 0.21
$t\bar{t}W$	0.59 ± 0.11
$t\bar{t}Z$	0.48 ± 0.09
VVV	0.01 ± 0.00
Z + jets	0.15 ± 0.10
$t\bar{t}\gamma$	0.16 ± 0.08
W + jets	0.17 ± 0.13
Total Bkg.	8.5 ± 2.6
Signal	8.5 ± 0.7
S/B	$(100 \pm 32)\%$
Data	8

Table C.1: Pre-Fit Yields in the Signal Region including all uncertainties.

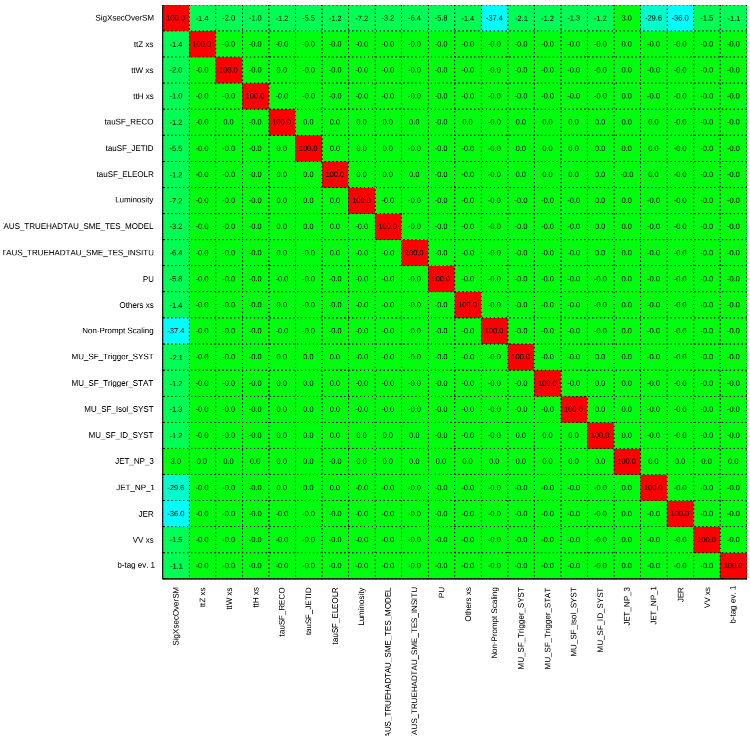

Figure C.1: Correlations among nuisance parameters as measured by a signal plus background fit on Asimov data. Only NPs with at least one correlation entry larger than 1% are shown.

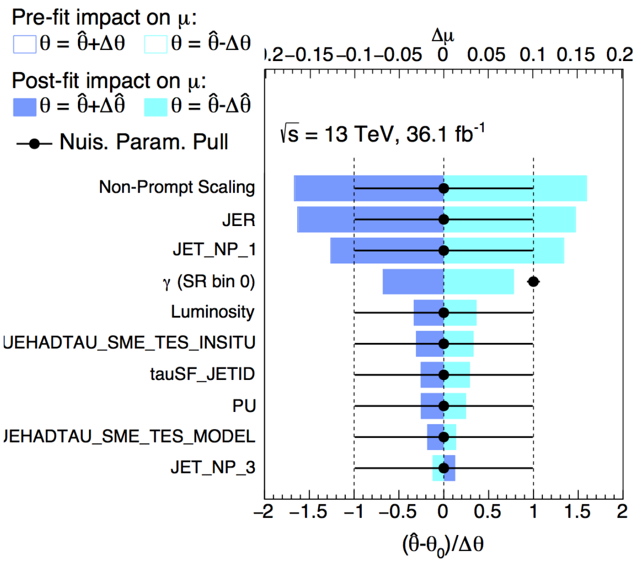

(a)

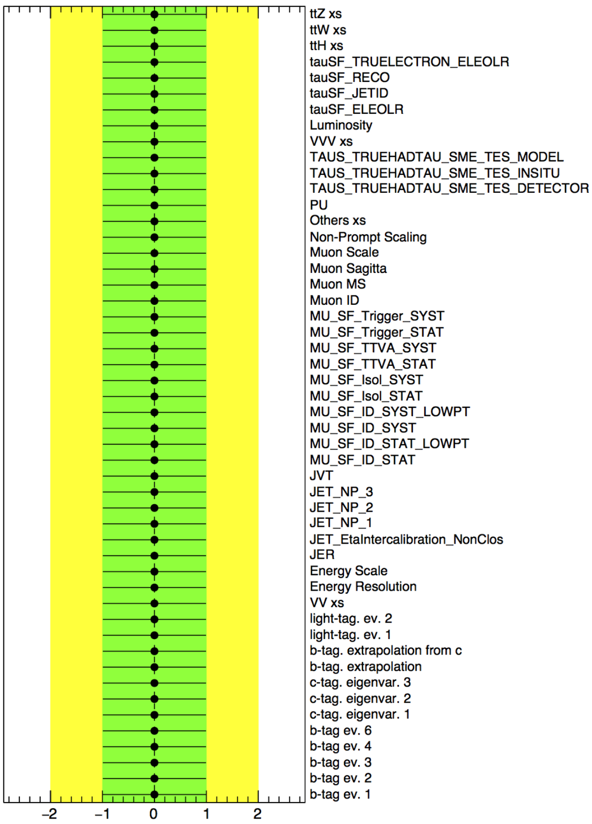

(b)

Figure C.2: (a)Ranking and pulls of the nuisance parameters as measured by signal plus background fits on Asimov data

APPENDIX D

Non-Prompt Systematics in the Validation Region

The systematic uncertainty from the ABCD method is introduced in the Validation Region on non-prompt MC background events and the kinematic distributions corresponding to those presented in Figures 5.1 of Chapter 5 are shown here. As expected, the inclusion of a systematic enables the data points to lie within the uncertainty bands.

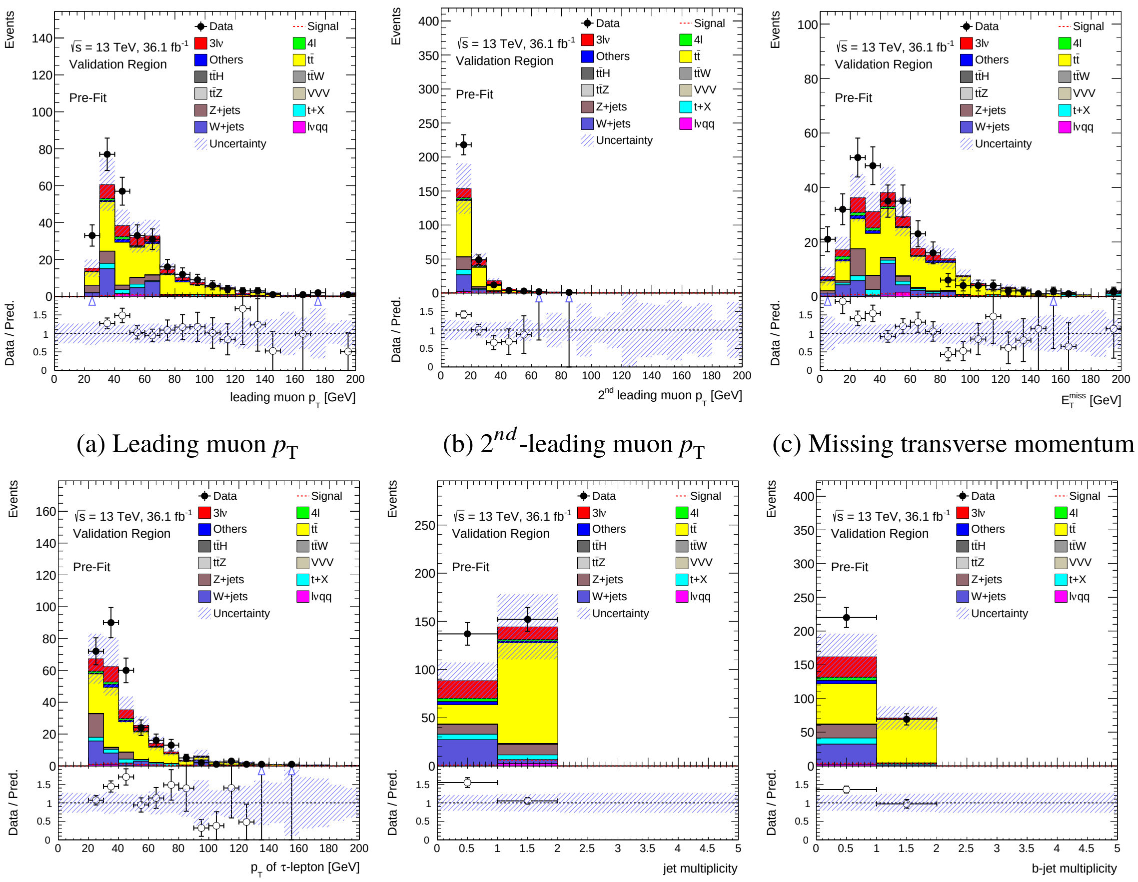

(a) Leading muon p_T (b) 2^{nd}-leading muon p_T (c) Missing transverse momentum

(d) τ-lepton p_T (e) Jet multiplicity (f) b-jet multiplicity

Figure D.1: Kinematic distributions of MC vs. data in the Validation Region including systematic uncertainties from non-prompt background estimation. Last bins of figures (a) and (c) contain overflow.

List of Figures

List of Tables